Contrib Mineral Petrol (2012) 164:261–280
DOI 10.1007/s00410-012-0737-5

ORIGINAL PAPER

A parameterized model for REE distribution between low-Ca pyroxene and basaltic melts with applications to REE partitioning in low-Ca pyroxene along a mantle adiabat and during pyroxenite-derived melt and peridotite interaction

Lijing Yao · Chenguang Sun · Yan Liang

Received: 27 September 2011 / Accepted: 3 March 2012 / Published online: 29 March 2012

Abstract Low-Ca pyroxenes play an important role in mantle melting, melt-rock reaction, and magma differentiation processes. In order to better understand REE fractionation during adiabatic mantle melting and pyroxenite-derived melt and peridotite interaction, we developed a parameterized model for REE partitioning between low-Ca pyroxene and basaltic melts. Our parameterization is based on the lattice strain model and a compilation of published experimental data, supplemented by a new set of trace element partitioning experiments for low-Ca pyroxenes produced by pyroxenite-derived melt and peridotite interaction. To test the validity of the assumptions and simplifications used in the model development, we compared model-derived partition coefficients with measured partition coefficients for REE between orthopyroxene and clinopyroxene in well-equilibrated peridotite xenoliths. REE partition coefficients in low-Ca pyroxene correlate negatively with temperature and positively with both calcium content on the M2 site and aluminum content on the tetrahedral site of pyroxene. The strong competing effect between temperature and major element compositions of low-Ca pyroxene results in very small variations in REE partition coefficients in orthopyroxene during adiabatic mantle melting when diopside is in the residue. REE partition coefficients in orthopyroxene can be treated as constants at a given mantle potential temperature during decompression melting of lherzolite and diopside-bearing harzburgite. In the absence of diopside, partition coefficients of light REE in orthopyroxene vary significantly, and such variations should be taken into consideration in geochemical modeling of REE fractionation in clinopyroxene-free harzburgite. Application of the parameterized model to low-Ca pyroxenes produced by reaction between pyroxenite-derived melt and peridotite revealed large variations in the calculated REE partition coefficients in the low-Ca pyroxenes. Temperature and composition of starting pyroxenite must be considered when selecting REE partition coefficients for pyroxenite-derived melt and peridotite interaction.

Keywords REE partition coefficient · Orthopyroxene · Subcalcic augite · Low-Ca pyroxene · Lattice strain model · Adiabatic mantle melting · Pyroxenite-derived melt and peridotite interaction

Communicated by T. L. Grove.

Electronic supplementary material The online version of this article (doi:10.1007/s00410-012-0737-5) contains supplementary material, which is available to authorized users.

L. Yao · C. Sun · Y. Liang (✉)
Department of Geological Sciences, Brown University, Providence, RI 02912, USA
e-mail: Yan_Liang@brown.edu

Introduction

The Earth's upper mantle is mainly composed of olivine and pyroxene. Due to their relative high affinity for incompatible trace elements, clinopyroxene (cpx) and orthopyroxene (opx) play an important role in trace element fractionation during partial melting and melt migration in the upper mantle. Pyroxene-melt trace element partition coefficient is a key parameter for constraining these processes. Considerable progress has been made in understanding trace element partitioning between cpx and basaltic melts (e.g., Wood and Blundy 2003 and references therein). However, orthopyroxene becomes the dominant phase to fractionate incompatible trace elements when cpx

is consumed during late-stage melting of a peridotite or during melting of a lunar cumulate mantle composed of olivine and opx (e.g., Snyder et al. 1992). Furthermore, an opx-rich lithology can also be formed during melting of a marble cake mantle that consists of pyroxenite embedded in a lherzolite host at high pressure. During mantle upwelling, pyroxenite starts to melt at greater depth than peridotite (e.g., Takahashi and Nakajima 2002; Pertermann and Hirschmann 2003a; Hirschmann et al. 2003; Spandler et al. 2008). In general, pyroxenite-derived melts are more silica-rich and, when reacting with their surrounding lherzolite, can produce low-Ca pyroxene-enriched lithologies such as orthopyroxenite and harzburgite (Yaxley and Green 1998; Takahashi and Nakajima 2002; Morgan and Liang 2005; Lo Cascio and Liang 2007; Lo Cascio 2008). The low-Ca pyroxene includes both opx and subcalcic augite and is produced at the expense of cpx and olivine in the lherzolite. Compared with opx in the unreacted lherzolite, this layer of low-Ca pyroxene has higher Ca and Al contents and a lower Mg# ($100 \times \mathrm{Mg}/(\mathrm{Mg} + \mathrm{Fe})$, in molar fraction). These low-Ca pyroxenes could have different trace element partition coefficients (D) from opx in the unreacted lherzolite given the distinct chemical compositions. One of the main objectives of this study is to determine the partition coefficients of trace elements in the low-Ca pyroxenes derived from the melt-rock reaction.

In general, mineral-melt trace element partition coefficients (D_j) from a given partitioning experiment vary systematically as a function of their ionic radii and temperature and can be quantitatively described by the lattice strain model (Brice 1975; Blundy and Wood 1994; Wood and Blundy 1997):

$$D_j = D_0 \cdot \exp\left\{\frac{-4\pi E N_A}{RT}\left[\frac{r_0}{2}\left(r_j - r_0\right)^2 + \frac{1}{3}\left(r_j - r_0\right)^3\right]\right\} \quad (1)$$

where D_0 is the mineral-melt partition coefficient for the strain-free substitution; r_0 is the radius of a hypothetical cation that substitutes into the site with zero strain; r_j is the ionic radius of the element of interest; E is the effective Young's modulus for the lattice site; N_A is Avogadro's number; R is the gas constant; and T is temperature in Kelvin. Applications of the lattice strain model to rare earth element (REE) partitioning between cpx and basaltic melt have been summarized in Wood and Blundy (1997, 2002), and a recent update can be found in Sun and Liang (2012).

Compared with cpx, there are considerably fewer trace element partitioning data for low-Ca pyroxenes. Of the published low-Ca pyroxene partitioning data, there are large variations in selected trace elements (e.g., $D_{\mathrm{La}} = 0.00004$–$0.054$, $D_{\mathrm{Nd}} = 0.0005$–0.114, $D_{\mathrm{Yb}} = 0.0202$–0.449; sources of data are given in Table 3 plus those from Colson et al. 1988; Kennedy et al. 1993; Klemme et al. 2006). It is not clear which set of the published partition coefficients one should use for low-Ca pyroxene when modeling adiabatic mantle melting or melt-rock reaction. Based on the published experimental data and the lattice strain model, Wood and Blundy (2003) proposed a preliminary model to describe REE partitioning between opx and melt. Due to the limited partitioning data, they set the effective Young's modulus E to a constant value of 360 GPa and D_0 a factor of five lower than that in cpx. Their model generally underestimates the REE partition coefficients in well-equilibrated opx by a factor of up to 5 and cannot be applied to subcalcic augite (Fig. 1a). Bédard (2007) compiled published opx partition coefficients from both partitioning experiments and natural samples. Based on linear regression analyses, he suggested that ln(D) for a given REE could be calculated using the ln(MgO) of the melt, the Mg# of opx, the SiO_2 content in the melt, or a combination of these variables. Bédard (2007) provided five different partitioning models for each element, of which a linear function based on the ln(MgO) of the melt and another based on the Mg# of opx appear to give better predictions of D_{REE}. We compared these two models and found that the linear functions based on ln(MgO) of the melt (Fig. 1b) generated better predictions than those based on the Mg# of opx (Fig. 1c); however, neither model is applicable to REE partitioning in subcalcic augite (Fig. 1b, c). Witt-Eickschen and O'Neill (2005) and Lee et al. (2007) developed models for REE partitioning between opx and cpx in peridotite. Orthopyroxene-melt partition coefficients may be deduced from their models given cpx-melt partition coefficients. However, their models were based on the analysis of peridotite xenoliths that were equilibrated at subsolidus conditions, and extrapolation to magmatic conditions needs further examination. Hence, an accurate model is needed to quantitatively describe REE partitioning in low-Ca pyroxenes.

Sun and Liang (2012) developed a new parameterized lattice strain model for REE and Y partitioning between cpx and basaltic melt. Instead of using all or most of the published cpx-melt partitioning data in the literature, they selected a subset of data from 43 partitioning experiments (a total of 344 data) that show no obvious signs of chemical disequilibrium and that were analyzed by either ion probe or laser-ablation inductively coupled plasma mass spectrometry (LA-ICP-MS). They then systematically examined the effects of temperature (T), pressure (P), and mineral and melt compositions (X) on REE and Y partitioning in cpx. Through an extensive search of various permutations of the composition variables, they found that Mg content on the M2 site ($X_{\mathrm{Mg}}^{\mathrm{M2}}$) and Al content on the tetrahedral site (X_{Al}^{T}) in cpx, the molar fraction of water in

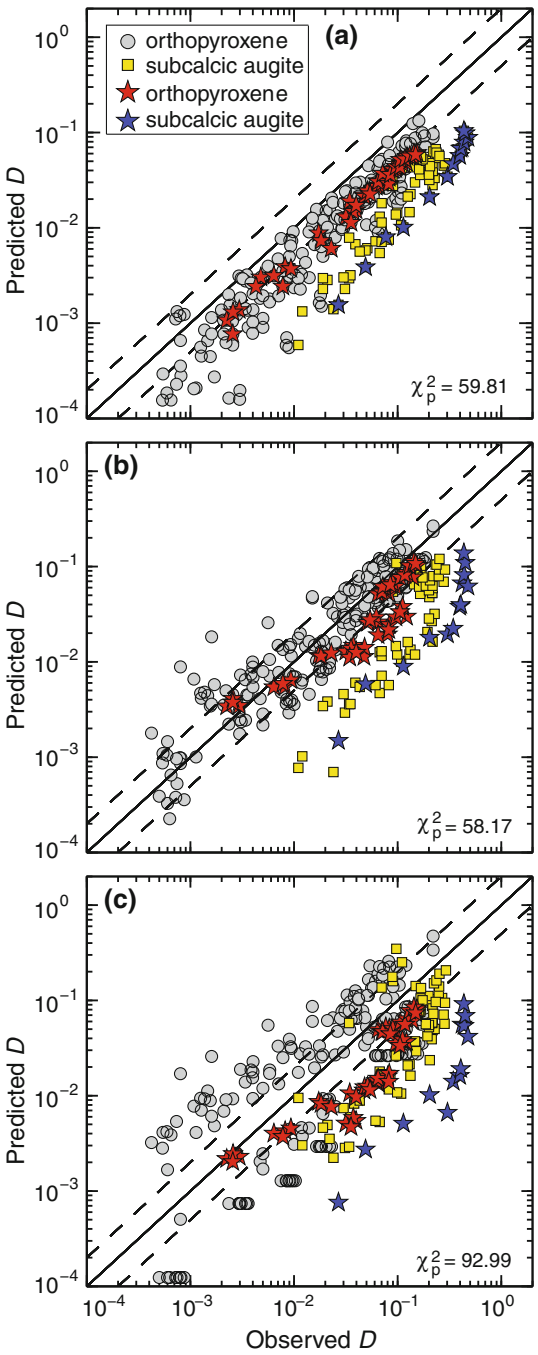

Fig. 1 Comparison between model-predicted low-Ca pyroxene partition coefficients and observed values. Observed values are from partitioning experiments listed in Table 3. Predicted values are calculated using the preliminary model of Wood and Blundy (2003), (**a**), and two models from Bédard (2007) based on ln(MgO) of melt (**b**) and Mg# of opx (**c**). The *solid line* represents 1:1 ratio, and *dashed lines* represent 2:1 and 1:2 ratios, respectively. χ^2_P is the Pearson's chi-square calculated according to Eq. (10). *Circles* and *squares* are the published data; *stars* are new experimental results of this study

the melt ($X^{melt}_{H_2O}$), and T were the primary variables determining D_0. X^{M2}_{Mg} and Al content on the M1 site (X^{M1}_{Al}) in cpx are the main factors affecting r_0. They showed, through a simultaneous inversion of the 344 filtered partitioning data, that the following expressions for the lattice strain parameters gave an excellent fit to the observed data:

$$\ln D_0 = -7.14(\pm 0.53) + \frac{7.19(\pm 0.73) \times 10^4}{RT} + 4.37(\pm 0.47)X^T_{Al} + 1.98(\pm 0.36)X^{M2}_{Mg} - 0.91(\pm 0.19)X^{melt}_{H_2O} \quad (2)$$

$$r_0 = 1.066(\pm 0.007) - 0.104(\pm 0.035)X^{M1}_{Al} - 0.212(\pm 0.033)X^{M2}_{Mg} \quad (3)$$

$$E = [2.27(\pm 0.44)r_0 - 2.00(\pm 0.44)] \times 10^3 \quad (4)$$

where $R = 8.3145$ J mol^{-1} K^{-1} and numbers in parentheses are two standard deviations calculated directly from the inversion. Using residual cpx compositions calculated along a mantle adiabat derived from pMELTS (Ghiorso et al. 2002) and Eqs. (1)–(4), they demonstrated that competing effects between temperature and cpx compositions gave rise to nearly constant partition coefficients for REE and Y in residual cpx in spinel lherzolite stability field along a mantle adiabat (see also supplementary Fig. S1). The modeling and conclusions from Sun and Liang (2012) are intriguing and raise two broader questions: (1) Can a similar approach be used for modeling REE and Y partitioning in low-Ca pyroxenes? (2) Do similar partitioning behaviors exist in the low-Ca pyroxenes during adiabatic mantle melting?

There are considerably fewer REE and Y partitioning data for low-Ca pyroxene than those for cpx. In this study, we report new trace element partitioning data for low-Ca pyroxenes produced by reactions between pyroxenite-derived melt and lherzolite at 1,340–1,425 °C and 2 GPa. Following a procedure similar to that of Sun and Liang (2012), we then develop a parameterized lattice strain model for REE and Y partitioning in low-Ca pyroxenes. As an independent test of our new parameterization, we compute the REE partition coefficients between opx and cpx in peridotite xenoliths using major element compositions reported in the literature, and the REE partitioning models for cpx in Sun and Liang (2012) and low-Ca pyroxenes in this study. There is an excellent agreement between our model-derived opx-cpx partition coefficients for REE and those directly measured by LA-ICP-MS. As examples of geochemical application, we investigate the variation of REE and Y partitioning in low-Ca pyroxenes produced by pyroxenite-derived melt and peridotite interaction using major element compositions of the minerals reported in the melt-rock reaction experiments. Finally, we show that variations of opx-melt partition coefficients for REE are relatively small during adiabatic mantle melting and that constant partition coefficients can be used in studies of decompressional melting of lherzolite and cpx-bearing harzburgite.

Experiment

Experimental strategy and setup

Partial melting and melt-rock reaction experiments have shown that major element compositions of pyroxenite-derived melt vary considerably (gray fields in Fig. 2) and overlap with a significant number of low-Ca pyroxene-melt partitioning experiments (orange squares in Fig. 2). To further expand the database for trace element partitioning in low-Ca pyroxene, we conducted a set of pyroxenite-derived melt and peridotite reaction experiments. These experiments produced large, low-Ca pyroxene crystals that are well suited for partitioning studies. Figure 3 shows the experimental setup that consists of a melt layer (basaltic andesite or diorite) at the top, a layer of melt-lherzolite mixture in the middle, and a lherzolite layer at the bottom, in volume proportions of approximately 2:2:1. The mixture consists of two parts of melt and one part of lherzolite. Based on the basaltic andesite and lherzolite dissolution experiments of Morgan and Liang (2005) and Lo Cascio (2008), the reaction between lherzolite and a silica-saturated melt at temperatures above the solidus of lherzolite results in the dissolution of cpx and olivine and the precipitation of low-Ca pyroxene. The mixed layer in the middle helps to establish full contact between melt and lherzolite, facilitating the melt-peridotite reaction. If the temperature at the top of the reaction couple is slightly colder than that in the middle of the charge, which is normally achieved in a piston cylinder apparatus, large low-Ca pyroxene crystals will precipitate at the cold end of the capsule. Dissolution, precipitation, and reprecipitation

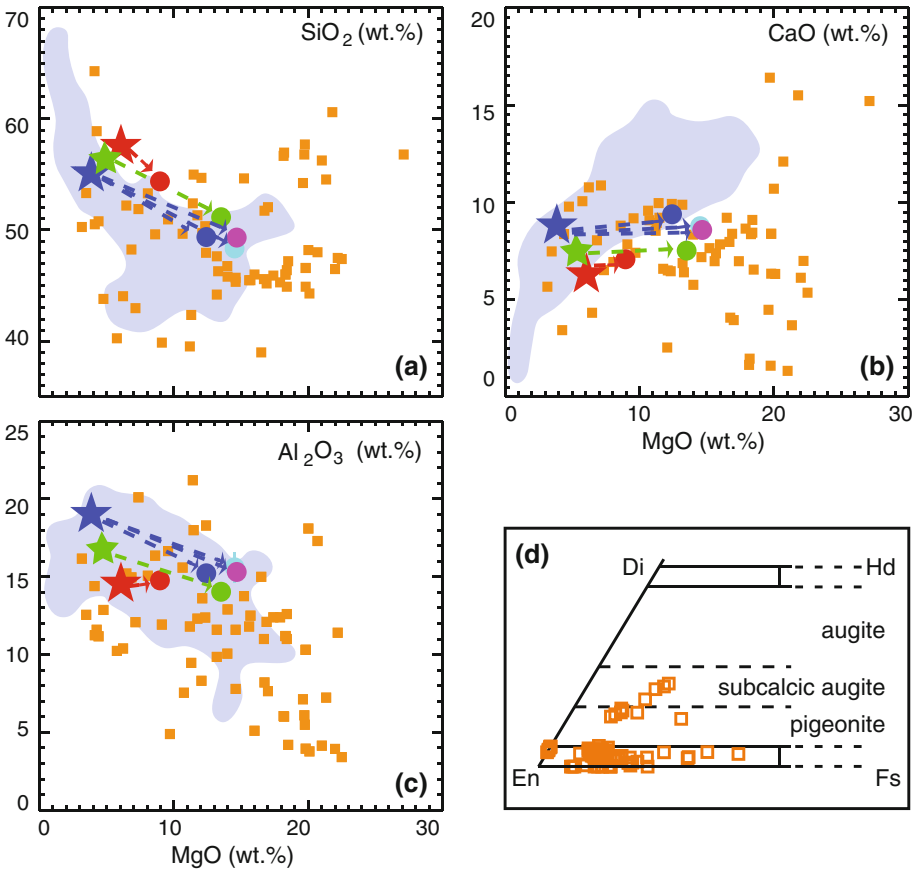

Fig. 2 Compositions of melt from pyroxenite and ecologite partial melting studies and low-Ca pyroxene partitioning experiments (**a**–**c**), and quadrilateral projection of the low-Ca pyroxene compositions in the corresponding partitioning experiments (**d**). The *gray fields* in (**a**–**c**) are the melt compositions from selected pyroxenite and eclogite melting studies (Takahashi et al. 1998; Yaxley and Green 1998; Rapp et al. 1999; Klemme et al. 2002; Takahashi and Nakajima 2002; Kogiso et al. 2003; Hirschmann et al. 2003; Pertermann and Hirschmann 2003b; Keshav et al. 2004; Kogiso and Hirschmann 2006; Spandler et al. 2008; Yaxley and Sobolev 2007; Lambart et al. 2009). Orange squares represent melts from low-Ca partitioning experiments (sources of data are listed in Table 3 plus those from Colson et al. 1988; Kennedy et al. 1993; Klemme et al. 2006). Larger symbols in (**a**–**c**) represent melt compositions from this study: *Stars* are starting compositions of FS3-1 (*red*), basaltic andesite Mont 147 (*blue*), and FS3-1-T1 (*green*, estimated, a mixture of FS3-1 and Mont 147). *Circles* are the compositions of melt from runs BA1LH2-T4 (*cyan*), BA1LH2-T5 (*blue*), BA1LH2-T6 (*magenta*), FS3-1-T1 (*green*), and DA1LH2-T2 (*red*) in this study. Dashed lines connect the starting and final melt compositions

in a nearly homogeneous melt along a small temperature gradient led to the formation of a few large pyroxene crystals near the top of the reaction couple.

Starting materials

Natural sample powders were used in our experiments for both melt and lherzolite. Based on the earlier work of Morgan and Liang (2005) and Lo Cascio (2008), we chose a basaltic andesite (Mont 147) and a diorite (FS3-1) to represent pyroxenite-derived melts (blue and red stars in Fig. 2, respectively). Sample Mont 147 (provided by Dr. J.D. Devine) is from Montserrat and used by Morgan and Liang (2005) in their studies of melt-lherzolite reactions at 1,300 °C and 1 GPa. Sample FS3-1 (provided by Dr. W. Xu) is from a diorite intrusion in the North China craton. The starting lherzolite powder (KBH-1Y) was created by mixing fine-grained optically clean diopside (15 wt%), opx (30 %), olivine (52 %), and spinel (3 %) that are from a spinel lherzolite xenolith from Kilbourne Hole, NM (sample KBH-1 used in Morgan and Liang 2005). The mixtures were crushed in an agate mortar and ground under ethanol twice for 40 min each and then stored in an oven at 110 °C to minimize the adsorption of water. Major element compositions of the starting materials are listed in Table 1.

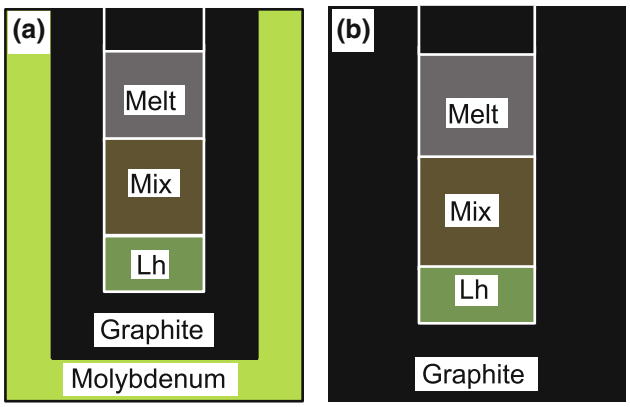

Fig. 3 Schematic diagrams showing the reaction couple setups. Graphite-lined molybdenum double capsules (**a**) were used for run BA1LH2-T5, BA1LH2-T6, FS3-1-T1, and DR1LH2-T2; and a graphite capsule (**b**) was used for run BA1LH2-T4. The volume proportion of the three layers is approximately 2:2:1, from top to bottom. Lh stands for lherzolite; Mix is the mixture of basaltic melt and lherzolite

Experimental procedure

Experiments were performed in a 19.05-mm piston cylinder apparatus at Brown University. The experimental assembly consisted of a salt-Pyrex® sleeve, a straight-wall graphite furnace, and internal spacers of crushable MgO. Of the five experiments reported in this study, four were run using a graphite-lined molybdenum (Mo) capsule and one using a graphite capsule. The length of the capsules varies from ~5 mm to ~10 mm. The furnace assembly was vacuum-dried at 200 °C overnight and stored at 110 °C. Experiments were conducted using the "hot piston-in" technique. To start an experiment, we first pressurized the charge to a pressure that is slightly below

Table 1 Major element composition of starting materials for the partitioning experiments

Oxide	Basaltic andesite[a]	Diorite[b]	Olivine[c]	Orhopyroxene[c]	Clinopyroxene[c]	Spinel[c]
SiO_2 (wt%)	55.09	57.55	40.47	54.25	51.82	0.09
TiO_2	0.79	0.47	0.01	0.11	0.29	0.15
Al_2O_3	19.03	14.54	0.1	5.43	6.98	57.88
Cr_2O_3	n.a.	n.a.	0.06	0.56	0.91	10.87
FeO*	8.42	6.38	9.21	5.57	3.42	10.44
NiO	n.a.	n.a.	0.23	0.09	0.05	n.a.
MnO	0.22	0.1	0.14	0.13	0.11	0.12
MgO	3.86	6.06	49.8	32.87	18.76	21.21
CaO	8.8	6.29	0.2	1.58	16.94	n.a.
Na_2O	2.97	4.19	0.01	0.16	1.07	n.a.
K_2O	0.71	2.37	n.a.	n.a.	n.a.	n.a.
P_2O_5	0.13	0.21	n.a.	n.a.	n.a.	n.a.
Total	100.01	99.54	100.22	100.75	100.35	100.86
Mg#	44.96	64.19	90.61	91.32	90.72	78.53

[a] Mont 147, provided by Dr. J.D. Devine, used in Morgan and Liang (2005)

[b] FS3-1 from North China craton, provided by Dr. W. Xu

[c] compositions from Lo Cascio (2008)

n.a. not analyzed, FeO* total Fe in FeO

Table 2 Pyroxene-melt partition coefficients calculated from LA-ICP-MS analysis

Run No.	BA1LH2-T4	BA1LH2-T5	BA1LH2-T6	FS3-1-T1	DR1LH2-T2
P (GPa)	2	2	2	2	2
T (°C)	1,425	1,425	1,425	1,380	1,340
Dur (h)	48	48	77	48	48
D	opx/melt	opx/melt	opx/melt	opx/melt	sub.aug/melt
Na	0.087 (12)	0.096 (2)	0.078 (3)	0.064 (5)	0.246 (17)
P	0.090 (26)	–	0.0812 (47)	–	–
K	–	–	–	–	0.0028 (1)
Li	–	0.379 (23)	–	0.286 (49)	0.415 (44)
Sc	0.76 (7)	0.752 (39)	0.619 (49)	0.728 (49)	1.42 (7)
Ti	0.124 (15)	0.117 (5)	0.098 (14)	0.114 (8)	0.175 (27)
V	1.74 (16)	1.74 (11)	1.34 (15)	1.55 (7)	3.47 (21)
Cr	4.13 (35)	3.68 (14)	3.58 (38)	3.80 (25)	7.8 (5)
Mn	0.86 (8)	0.934 (17)	0.776 (18)	0.964 (32)	1.67 (8)
Co	1.30 (12)	1.333 (43)	1.105 (23)	1.341 (36)	1.45 (7)
Ni	4 (1)	2.52 (11)	2.17 (9)	2.85 (19)	3.13 (21)
Cu	–	0.0547 (34)	0.0426 (29)	–	–
Zn	0.65 (9)	0.72 (2)	0.63 (3)	0.704 (36)	0.677 (43)
Sr	–	0.00263 (18)	–	0.0025 (5)	0.053 (7)
Y	0.083 (11)	0.0769 (26)	0.065 (8)	0.071 (6)	0.419 (44)
Zr	0.0212 (35)	0.0186 (11)	0.0158 (31)	0.0149 (15)	0.048 (8)
La	0.00165 (46)	–	–	–	0.0268 (45)
Ce	0.0030 (6)	0.00258 (35)	0.0022 (6)	0.00257 (47)	0.049 (8)
Pr	0.0048 (8)	–	0.0043 (6)	–	0.077 (10)
Nd	0.0082 (12)	0.0093 (9)	0.0064 (14)	0.0078 (9)	0.114 (21)
Sm	0.0173 (29)	–	0.018 (6)	0.023 (11)	0.204 (36)
Eu	0.0187 (40)	–	0.0129 (28)	–	0.174 (31)
Tb	0.047 (8)	0.01 (1)	0.0345 (36)	0.040 (5)	0.344 (41)
Gd	0.040 (7)	0.037 (7)	0.0316 (42)	0.0355 (44)	0.303 (39)
Dy	0.066 (8)	0.0622 (27)	0.051 (7)	0.054 (8)	0.40 (6)
Ho	0.080 (11)	0.083 (8)	0.065 (15)	0.082 (6)	0.41 (6)
Er	0.096 (16)	0.090 (7)	0.072 (15)	0.085 (11)	0.44 (5)
Tm	0.122 (17)	0.112 (18)	0.096 (15)	0.105 (16)	0.48 (6)
Yb	0.140 (20)	0.123 (14)	0.106 (14)	0.117 (13)	0.45 (5)
Lu	0.153 (24)	0.144 (24)	0.131 (29)	0.149 (11)	0.435 (35)
Hf	0.039 (11)	0.0348 (49)	0.026 (7)	0.030 (8)	0.097 (9)
Ta	0.00150 (38)	0.00112 (6)	0.00121 (47)	0.0013 (5)	0.0077 (34)
Pb	–	–	0.0022 (8)	0.0018 (8)	0.013 (5)

Numbers in parenthesis represent one standard deviation

opx orthopyroxene, *sub. aug* subcalcic augite

2 GPa. The temperature was then increased to the target temperature at a rate of 75 °C per minute while slowly increasing the pressure to the target pressure. The run was held at the specified temperature and pressure for 48–72 h before quenching to room temperature (Table 2). The retrieved capsule was sectioned longitudinally, mounted in epoxy, and polished to 1 μm finish.

The nominal pressure was not corrected for friction. No pressure correction was applied to the measured electromotive force (*e.m.f.*). Temperature was measured using a $W_{97}Re_3$–$W_{75}Re_{25}$ thermocouple and controlled with a Eurotherm 818. Uncertainties in temperature measurements are about ±10 °C. The oxygen fugacity of the experimental conditions is estimated to be close to or

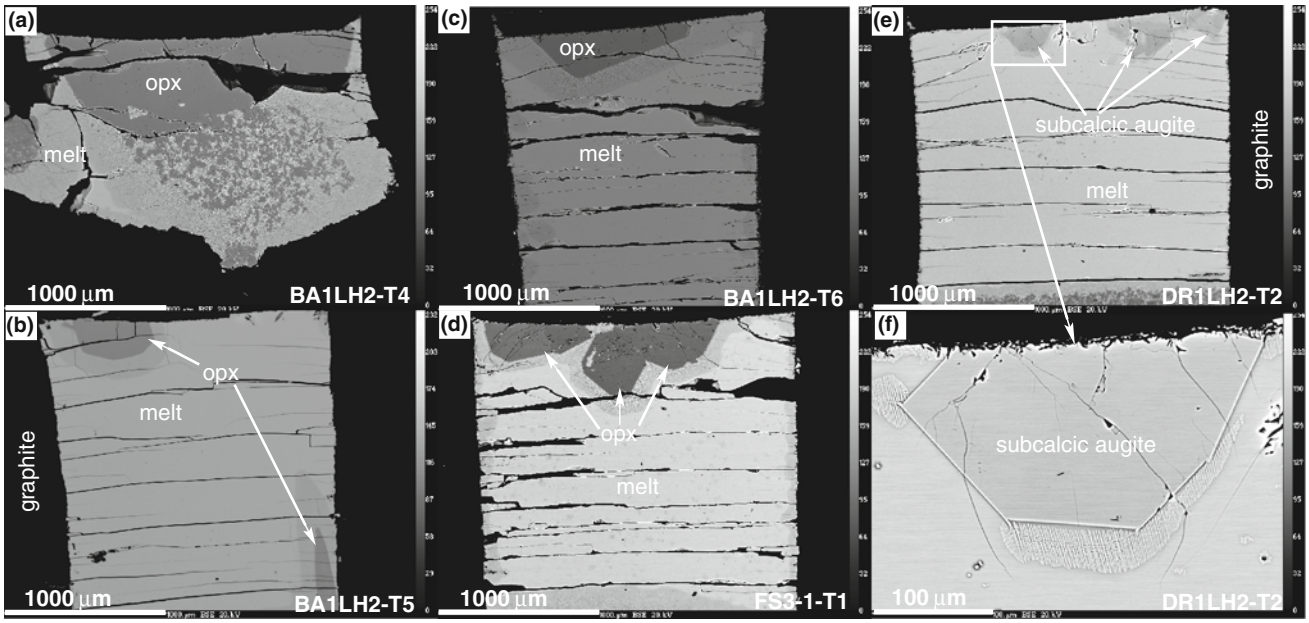

Fig. 4 Back-scattered electron images of the experimental charges showing large opx (**a**–**d**) or subcalcic augite (**e**) crystals. A close-up view of a subcalcic augite crystal from (**e**) is shown in (**f**). Medium *gray layers* around crystals in (**b**–**d**) are quench growth. Expanded views of selected runs are shown in supplementary Fig. S2

slightly more reducing than the carbon–carbon monoxide (CCO) buffer (Médard et al. 2008).

Analytical techniques

Major element compositions of the crystal and melt were analyzed using a Cameca SX100 electron microprobe at Brown University. For the glasses, we used an accelerating voltage of 15 kV, a beam current of 15 nA, and a beam size of 5 μm for samples BA1LH2-T4 and BA1LH2-T6, and we used an accelerating voltage of 20 kV, a beam current of 25 nA, and a beam size of 20 μm for the other samples. For the minerals, we used an accelerating voltage of 20 kV, a beam current of 25 nA, and a beam size of 5 μm. Counting times were 10–30 s for peak and 10–15 s for background positions. Natural mineral standards were used, and the ZAF matrix correction was employed.

Trace element concentrations in crystals and glasses were measured in situ using a Thermo X-Series 2 quadrupole ICP-MS in conjunction with a New Wave UP 213 nm Nd-YAG laser-ablation system at the University of Rhode Island. The diameter of the laser beam was set to 60 μm for crystal and melt in run BA1LH2-T6 and crystal in run BA1LH2-T4, and 40 μm for crystals and melts in the other samples. Samples were ablated with an output energy of ~0.3 mJ at a frequency of 10 Hz. For each analysis, elements were analyzed in the mass spectrometer for a total time of 120 s. The background was measured for 30 s, and the signals were acquired for approximately 60 s by a laser firing. The gas mixture used during each analysis consisted of pure helium, which was used in the sample cell and later mixed downstream with pure argon. External standards used in the analyses include NIST-610 from Pearce et al. (1997), BCR-2g, BHVO-2g, and BIR-1g from Kelley et al. (2003), and GOR132, StH1s, T1, ML3B, and KL2 from Jochunm et al. (2006). Since MgO is the predominant major oxide in low-Ca pyroxene and its abundance is high in the reacted melt (Fig. 2), we used MgO as the internal standard. Electron microprobe analyses of MgO were chosen from points close to the spots analyzed by LA-ICP-MS. The detection limit for each analysis was estimated at 3 times or higher than the standard deviation of the background.

Experimental results

The experimental conditions and run products are summarized in Table 2, and representative back-scattered electron (BSE) images of the experimental charges are shown in Fig. 4 (BSE images showing the entire sectioned charges of selected runs can be found in supplementary Fig. S2). Subcalcic augites are observed in run DR1LH-T2 (Fig. 4e, f), whereas opx crystals are present in the other four runs. The experiments generally form a few large crystals on the top and along the sidewall of the graphite inner capsule (Fig. 4). The crystals are 300–1,500 μm in size. The low-Ca pyroxenes possess no obvious zoning or melt inclusions. Run FS3-1-T1 also has tiny opx crystals smaller than 10 μm in the lower part of the melt.

Major and trace element compositions of melt and pyroxenes are listed in supplementary Tables S1 and S2,

respectively. Melt from each experiment is relatively homogeneous; based on 9–17 spot analyses, standard deviations are smaller than the marker size in Fig. 2 for most experiments. There are some variations in Al_2O_3 content in melt of runs BA1LH2-T5 and BA1LH2-T6, which may be attributed to the thermal gradient within the charges. Major element compositions of pyroxene crystals are relatively homogeneous in each run.

The average trace element concentrations (weight fraction) in both the melt (C_j^{melt}) and the crystals ($C_j^{crystal}$) for each experiment (4–7 spots) are used to calculate partition coefficients:

$$D_j^{crystal} = \frac{C_j^{crystal}}{C_j^{melt}} \quad (5)$$

Partition coefficients are listed in Table 2 and graphically displayed according to element groups with increasing compatibility in Fig. 5. The partition coefficients of Sr fall in the range of published data, although D_K and D_{Pb} of subcalcic augite (DR1LH2-T2) have not been reported before. The partition coefficients of REE and Y show a systematic increase in compatibility with decreasing ionic radii. The small negative Eu anomalies presumably result from the reducing environment imposed by the Mo-graphite capsule. The partition coefficients of the high-field-strength elements (HFSE) and most of the transition metals (TM) in low-Ca pyroxene also show systematic variations in their compatibility and are comparable to the published data. The exception is D_{Cu} in opx, which is not within the range of the published data (Fig. 5). This may be attributed to either a paucity of published data, of which there are only two D_{Cu} values reported for opx, or a difference in the oxidation state. One D_{Cu} value for opx is from Adam and Green (2006), who reported a value of 2.8 in a hydrous garnet lherzolite. The other D_{Cu} value is from Klemme et al. (2006), who reported a value of 0.22 for enstatite in a simple system that is Ca-free. These two values may not adequately define the range of D_{Cu} for opx in the upper mantle. Alternatively, our experimental environment may be too reducing (c.f. Eu in Fig. 5), which results in a large fraction of Cu cations in the monovalent state (Cu^+). Sixfold coordinated Cu^+ has an ionic radius of 0.77 Å (Shannon 1976), which is larger than the M1 site of low-Ca pyroxene (ionic radius of Mg^{2+} is 0.72 Å), while Cu^{2+} (ionic radius of 0.73 Å) would be expected in Earth mantle. Overall, our measured trace element partition coefficients expand the range of low-Ca pyroxene trace element partition coefficients reported in the literature (Fig. 5).

REE and Y partitioning in pyroxene is mainly caused by substitution of the trivalent cations into the M2 site of pyroxene. For a given partitioning experiment, REE and Y partition coefficients generally follow a parabolic pattern in an Onuma diagram and can be described by the lattice strain model (Eq. 1). Here, we apply the lattice strain model to REE and Y partitioning data to obtain key parameters (D_0, r_0, and E in Eq. 1) for each experiment. For reasons outlined in the first section in "Discussion" below, we used the eightfold coordinated ionic radii of REE and Y from Shannon (1976) to fit the measured data while excluding Eu in the nonlinear regression analysis because of the possible presence of Eu^{2+} in our charges. The fitting results are summarized in Fig. 6, where data used in each regression analysis are shown as red circles. (In supplementary Fig. S3, we also show the fit to our experimental data using sixfold coordinated ionic radii and the lattice strain model.) The derived D_0 (0.248–0.658)

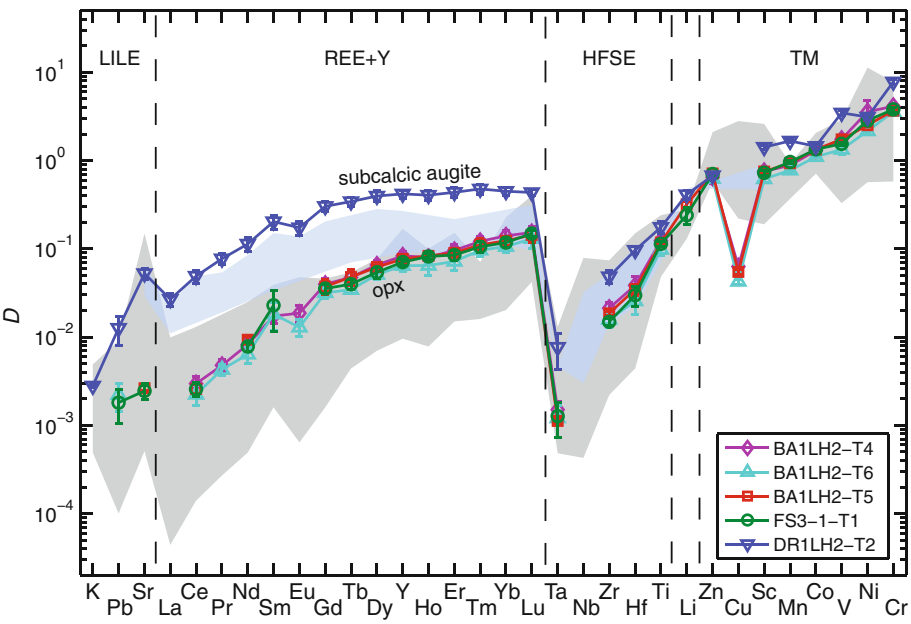

Fig. 5 Measured trace element partition coefficients, arranged in geochemical groups with increasing compatibility. LILE stands for large ion lithophile element; HFSE stands for high field strength element; TM stands for transition metal. The *gray field* represents the range of published partitioning data for opx; the *light blue field* represents the range of published partitioning data for subcalcic augite (sources of data are given in Table 3 plus those from Colson et al. 1988; Kennedy et al. 1993; Klemme et al. 2006)

from our experiments ranges to higher values than those we recalculated from the published partitioning experiments using eightfold coordinated ionic radii (0.05–0.464, except for D_0 of Green et al. 2000, which has a surprisingly high value of 3.27). The derived r_0 (0.781–0.984 Å) and E (152–292 GPa) from our experiments show relatively small variations than those we recalculated from the literature data (r_0 = 0.705–1.001 Å, and E = 110–427 GPa). Variations in the lattice strain parameters are due to variations in *P-T-X*, which we will discuss in the next section.

A parameterized model for REE and Y partitioning in low-Ca pyroxene

To better understand the *P-T-X* dependence of REE and Y partitioning in low-Ca pyroxene, we developed a parameterized model. Our parameterization is based on the lattice strain model using a subset of published partitioning data and follows the methodology of Sun and Liang (2012) for REE and Y partitioning between cpx and basaltic melts.

Data compilation

Although there is a fairly large database for REE and Y partitioning in low-Ca pyroxene from natural samples and experiments in the literature (see Bédard 2007 for a recent compilation), the quality of the published data is not uniform. Some data filtering is necessary to ensure the accuracy of the model. We compiled experimentally determined partition coefficients between low-Ca pyroxene and basaltic melt from the past two decades, to which we added the low-Ca pyroxene partitioning data from this study and the opx partitioning data for the lunar green, orange, and red picritic glass melts from Sun and Liang (manuscript in preparation, see also Sun et al. 2011). These data have been filtered on the basis of attainment of equilibrium (e.g., absence of core to rim variation, sector zoning in major elements, or melt inclusions, run duration), misfit or outlier with reference to the lattice strain model (e.g., Eu anomaly), and method of chemical analysis (LA-ICP-MS and ion probe), similar to the rational adopted by Sun and Liang (2012). REE and Y abundances in low-Ca pyroxenes are, in general, lower than

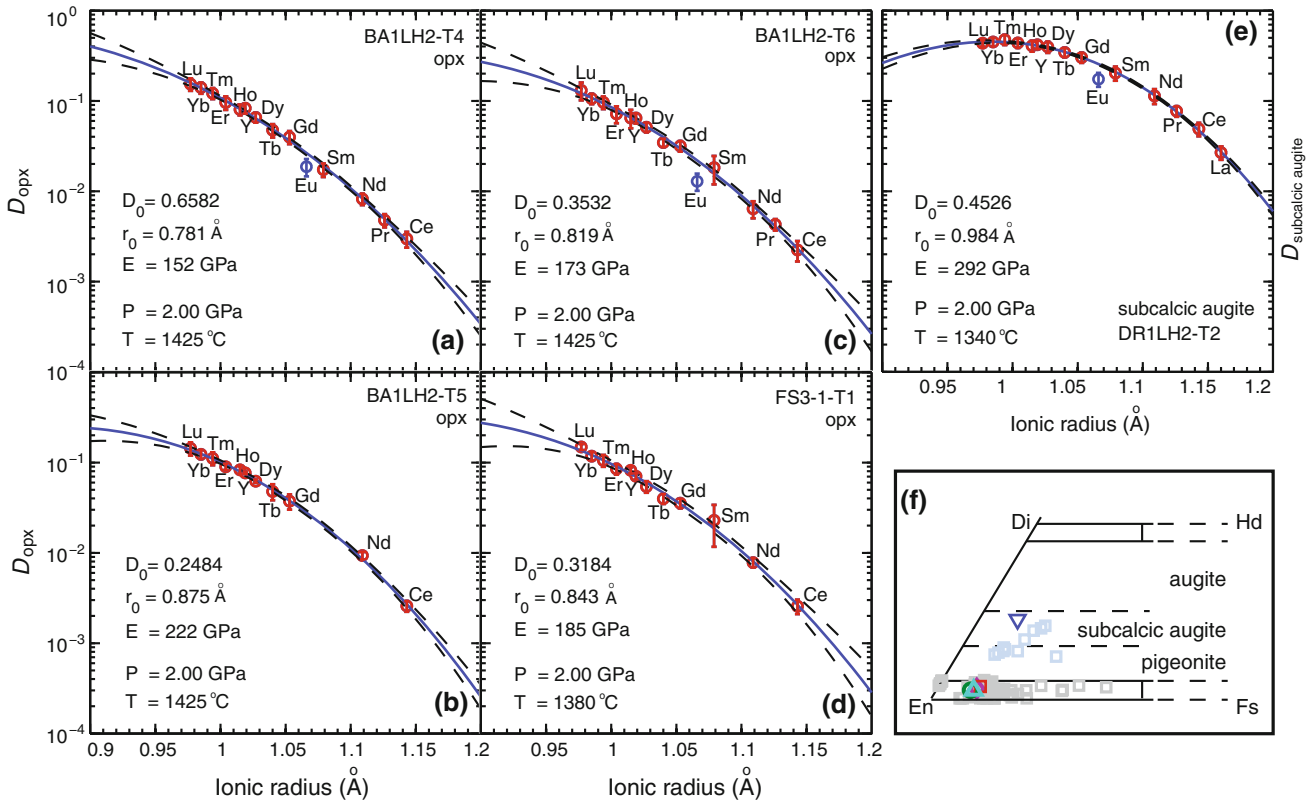

Fig. 6 Onuma diagrams showing the measured REE and Y partition coefficients between low-Ca pyroxene and melt as a function of ionic radii (**a**–**e**), and their corresponding major element projections in the pyroxene quadrilateral (**f**). *Red circles* in (**a**–**e**) are partitioning data used in the regression analyses; *blue circles* are Eu and excluded from the fit. *Error bars* represent one standard derivation of analyzed partitioning data. The *solid lines* in (**a**–**e**) represent the best-fit parabolas to the trivalent REE and Y in the M2 sites of pyroxene using Eq. (1). *Dashed lines* represent 95 % confidence intervals of the fit. Symbols in (**f**) are the same as those used in Fig. 5. For reasons outlined in the "Discussion", eightfold coordinated ionic radii from Shannon (1976) are used here. Similar Onuma diagrams using sixfold coordinated ionic radii are shown in the supplementary Fig. S3

Table 3 Data sources and experimental run conditions

Reference	N(n)[a]	*P* (GPa)	*T* (°C)	Dur (h)	Pyx	Pyx Mg#	$Ca^{M2}/6\text{-}O^{b}$	Melt Mg#	Melt SiO_2 (wt%)	Melt H_2O (wt%)
Ion probe analysis										
Frei et al. (2009)	5 (35)	1.1–3.2	1,230–1,535	24–144	opx	100	0.072–0.095	100	39.0–55.0	
van Kan Parker et al. (2010)	3 (21)	0.0001	1,326–1,390	60	opx	100	0.072–0.101	100	56.8–60.6	
Green et al. (2000)	1 (13)	2	1,080	46	opx	70	0.044	41	50.28	6.44
McDade et al. (2003a)	1 (8)	1.5	1,315	48	opx	91	0.074	83	47.95	
McDade et al. (2003b)	1 (6)	1.3	1,245	49	opx	90	0.073	72	49.67	1.64
Schwandt and MaKay (1998)	1 (8)	0.0001	1,210	120	opx	80	0.025	53	53.31	
Salters and Longhi (1999)	2 (14)	2.4–2.8	1,540–1,555	48	opx	90	0.062–0.067	72–73	45.9–46.3	
Salters et al. (2002)	1 (7)	3.4	1,660	19	opx	93	0.061	81	47.5	
Salters and Longhi (1999)	3 (21)	2.8	1,515–1,547	48	sub.aug	84–88	0.224–0.283	62–73	44.2–45.8	
Salters et al. (2002)	1 (7)	2.8	1,580	20.7	sub.aug	88	0.261	73	45.2	
van Westrenen et al. (2000)	1 (8)	3	1,538	21.5	sub.aug	73	0.225	55	47.6	
Tuff and Gibson (2007)	3 (39)	3	1,475–1,525	24	sub.aug	79–82	0.334–0.354	49–62	39.54–46.77	
Subtotal range	23 (187)	0.0001–3.4	1,080–1,660	19–144		70–100	0.025–0.354	41–100	39.0–60.6	
LA-ICP-MS										
Adam and Green (2006)	1 (10)	2.7	1,160	48	opx	84	0.051	64	39.88	9.9
van Kan Parker et al. (2011)	3 (18)	1.1–2.1	1,430–1,550	23–24	opx	84–87	0.028–0.040	62–70	46.0–47.4	
Sun and Liang in preparation	6 (66)	2–2.1	1,340–1,450	48–50	opx	77–81	0.058–0.079	48–56	32.57–45.33	
This study	4 (49)	2	1,380–1,425	48–77	opx	90–91	0.056–0.072	73–77	48.36–51.15	
This study	1 (14)	2	1,340	48	sub.aug	89	0.408	72	54.39	
Subtotal range	15 (157)	1.1–2.7	1,160–1,450	23–77		77–91	0.028–0.408	48–77	32.57–54.39	
Total range	38 (344)	0.0001–3.4	1,080–1,660	19–144		70–100	0.025–0.408	41–100	32.57–60.6	

Dur run duration, *Pyx* pyroxene, *opx* orthopyroxene, *sub. aug* subcalcic augite

[a] N stands for the number of experiments from the reference, and n in the parenthesis stands for the total number of elements from the experiments

[b] Molar content of Ca on the M2 site of pyroxene per six oxygen

those in cpx and hence more difficult to analyze using an electron microprobe, so we only considered data analyzed by ion probe or LA-ICP-MS in our parameterization. We obtained 344 data from 38 partitioning experiments for low-Ca pyroxene (29 for opx and 9 for subcalcic augite; 3 of the 29 opx experiments are conducted under hydrous conditions, Table 3), including 63 data from 5 experiments in the present study and 66 data from 6 experiments of Sun and Liang (in preparation). The size of the database is similar to that used by Sun and Liang (2012) for REE and Y partitioning in cpx (43 experiments and 344 data). In the online supplementary Figs. S4–S6, we show Onuma diagrams for the 38 experiments as well as those that were analyzed by either ion probe or LA-ICP-MS but excluded from our filtered database.

The 38 selected partitioning experiments cover a wide range of pressures (1 atm to 3.4 GPa) and temperatures (1,080–1,660 °C). These experiments produced low-Ca pyroxene and melt with large variations in composition (e.g., Ca content on the M2 site $X_{Ca}^{M2} = 0.025$–0.408, Mg# = 70–100 in pyroxene, Mg# = 41–100 in melt, SiO_2 = 39.0–60.6 wt% in melt; see Table 3 for details) and partition coefficients (e.g., $D_{La} = 0.0004$–0.0268, $D_{Nd} = 0.0016$–0.114, $D_{Yb} = 0.034$–0.449).

Parameterization method

To develop a parameterized model for REE and Y partitioning between low-Ca pyroxene and basaltic melt, we conducted a multivariable nonlinear least squares analysis.

Here, we followed the same procedure as described in Sun and Liang (2012) for the least squares analysis of REE and Y partitioning in cpx. The analysis involves two steps: (1) identification of the key parameters that affect D_0, r_0, and E in the lattice strain model through least squares analysis of individual experiments and (2) simultaneous inversion of all the filtered experimental data using the primary parameters identified in step (1).

As D_0 is the partition coefficient for strain-free substitution of the M2 site, we assume that D_0 has the same form used by Sun and Liang (2012) and that r_0 is a function of pyroxene compositions. Based on Monte Carlo simulations, Sun and Liang (2012) showed that E is positively correlated with r_0. We find three subparallel trends of E and r_0 for opx (squares), subcalcic augite (diamonds), and cpx (circles, Sun and Liang 2012) derived from regression analysis of individual partitioning experiments and the lattice strain model (Fig. 7). E and r_0 values of each pyroxene are positively correlated, which agrees with the Monte Carlo simulations of Sun and Liang (2012). The distribution of E and r_0 among the three subgroups of pyroxene reveals that E also correlates with pyroxene composition (e.g., Ca content on the M2 site, $X_{\mathrm{Ca}}^{\mathrm{M2}}$, and/or Mg content on the M2 site, $X_{\mathrm{Mg}}^{\mathrm{M2}}$). Accordingly, we assume E as a linear function of r_0, mineral and/or melt compositions.

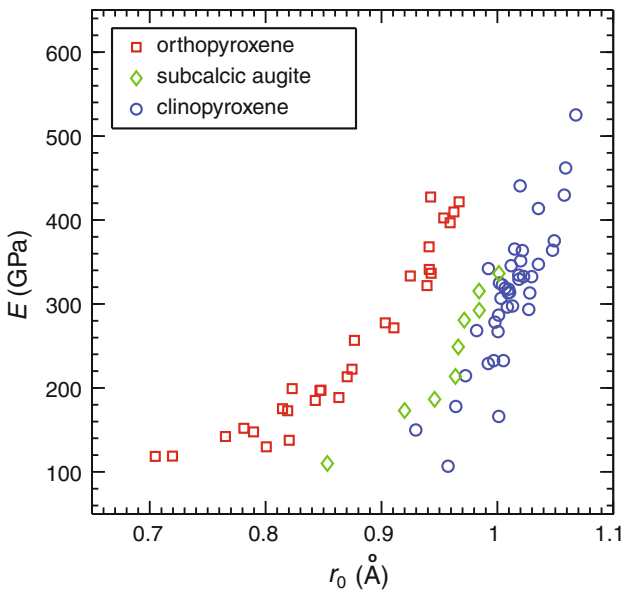

Fig. 7 Correlation between E and r_0 for the trivalent cations on the M2 site of pyroxenes. Each pair of E and r_0 is obtained by fitting REE and Y data from a partitioning experiment using the lattice strain model. Partitioning experiments for clinopyroxene are from the compilation of Sun and Liang (2012). Eightfold coordinated ionic radii from Shannon (1976) are used for both high-Ca and low-Ca pyroxenes

Through an extensive search of various permutations of the composition variables, we find that $X_{\mathrm{Ca}}^{\mathrm{M2}}$ and X_{Al}^{T} in low-Ca pyroxene and T are the primary variables that determine D_0, that $X_{\mathrm{Ca}}^{\mathrm{M2}}$ and $X_{\mathrm{Mg}}^{\mathrm{M2}}$ are the main factors affecting r_0, and that E can be described by a linear combination of r_0 and $X_{\mathrm{Ca}}^{\mathrm{M2}}$. Expressions for D_0, r_0, and E take the linear forms:

$$\ln D_0 = a_0 + \frac{a_1}{RT} + a_2 X_{\mathrm{Ca}}^{\mathrm{M2}} + a_3 X_{\mathrm{Al}}^{T} \tag{6}$$

$$r_0 = a_4 + a_5 X_{\mathrm{Ca}}^{\mathrm{M2}} + a_6 X_{\mathrm{Mg}}^{\mathrm{M2}} \tag{7}$$

$$E = a_7 + a_8 r_0 + a_9 X_{Ca}^{M2} \tag{8}$$

where a_0, a_1,…, a_9 are constant coefficients determined by stepwise multiple linear regression analyses of the lattice strain parameters (D_0, r_0, and E) and $X_{\mathrm{Ca}}^{\mathrm{M2}}$, X_{Al}^{T}, and $X_{\mathrm{Mg}}^{\mathrm{M2}}$ are cation numbers (per 6 oxygen) on respective sites in pyroxene.

To better constrain the low-Ca pyroxene-melt partitioning model for REE and Y, we substituted Eqs. (6)–(8) back into Eq. (1) and used the lattice strain model and our filtered partition coefficients to invert for the 10 fitting parameters, a_0, a_1… a_9, simultaneously through a global nonlinear least squares analysis (e.g., Seber and Wild 1989). To carry out the global inversion, we used the coefficients from the stepwise multiple linear regressions as initial values in the nonlinear least squares analysis and minimize the chi-square as defined below:

$$\chi^2 = \sum_{j=1}^{N} \left(\ln D_j - \ln D_j^m \right)^2 \tag{9}$$

where D_j is defined by Eq. (1) for element j, D_{j}^m is the measured opx-melt partition coefficient for element j, and N (=344) is the total number of measured partitioning data used in this study. Logarithmic normalized partition coefficients are used in the chi-square calculation because the absolute values of D are different from one element to another and systematic variations in REE abundances and partition coefficients are usually examined in normalized semi-log spider diagrams. Although convenient in nonlinear regression analysis, the absolute values of the chi-square defined in Eq. (9) depend on the number of data points used in the inversion and hence are not statistically meaningful. To quantitatively evaluate the goodness of the fit, we calculate the Pearson's chi-square for the estimation using the expression:

$$\chi_P^2 = \sum_{j=1}^{N} \frac{\left(D_j - D_j^m \right)^2}{D_j} \tag{10}$$

A better predictive model should produce a smaller χ_P^2. The results are shown in Fig. 8 and discussed below.

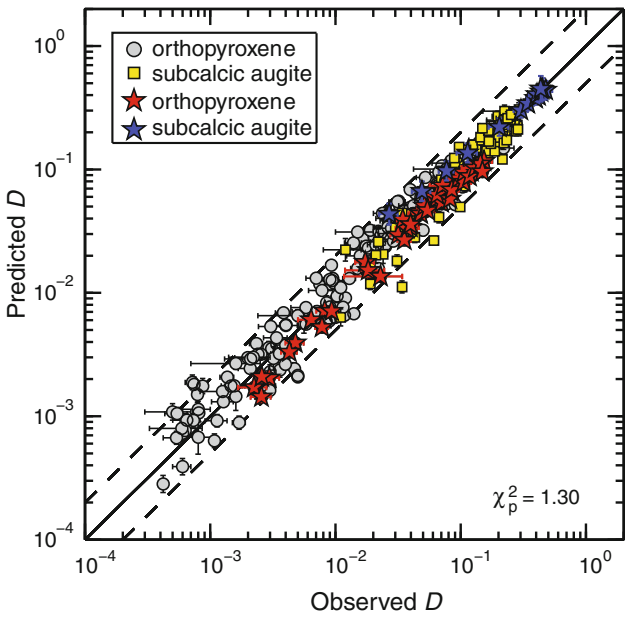

Fig. 8 Comparison between predicted partition coefficients calculated using the parameterized lattice strain model of Eqs. (1), (11)–(13) and the experimentally measured values. Data source and symbols are the same as those in Fig. 1

Model results

Results of the global fit to the 344 partitioning data from the 38 experiments (Table 3) using eightfold coordinated ionic radii from Shannon (1976) are as follows:

$$\ln D_0 = -5.37(\pm 0.49) + \frac{3.87(\pm 0.74) \times 10^4}{RT} + 3.56(\pm 1.02)X_{\mathrm{Ca}}^{\mathrm{M2}} + 3.54(\pm 0.61)X_{\mathrm{Al}}^{T} \quad (11)$$

$$r_0 = 0.69(\pm 0.05) + 0.43(\pm 0.15)X_{\mathrm{Ca}}^{\mathrm{M2}} + 0.23(\pm 0.06)X_{\mathrm{Mg}}^{\mathrm{M2}} \quad (12)$$

$$E = \left[-1.37(\pm 0.47) + 1.85(\pm 0.52)r_0 - 0.53(\pm 0.11)X_{\mathrm{Ca}}^{\mathrm{M2}}\right] \times 10^3 \quad (13)$$

where numbers in parenthesis are two standard deviations calculated directly from the simultaneous inversion. As D_0 determines the peak value of the parabola defined by Eq. (1), to the first order, the REE partition coefficients increase with increasing $X_{\mathrm{Ca}}^{\mathrm{M2}}$ and X_{Al}^{T} in low-Ca pyroxene but decrease with increasing temperature. In general, REE partition coefficients in subcalcic augite are larger than those in opx at a similar temperature and Al_2O_3 content.

Discussion

Combined with Eq. (1), Eqs. (11)–(13) provide a simple model for REE and Y partitioning between low-Ca pyroxene and basaltic melt. Figure 8 compares the predicted D values for REE and Y using Eqs. (1), (11)–(13) with the experimentally measured values. Almost all of the low-Ca pyroxene data fall between the 1:2 and 2:1 correlation lines (dashed lines in Fig. 8), including experimental results from the present study (stars). The small χ^2_P (=1.30) between observed and predicted D values suggests an excellent agreement between partitioning experiments and our model predictions. The χ^2_P value provided by our model is much smaller than that calculated using the preliminary model of Wood and Blundy (2003, $\chi^2_P = 59.81$, Fig. 1a) and the values derived from the models of Bédard (2007, $\chi^2_P = 58.17$ in Fig. 1b; and $\chi^2_P = 92.99$ in Fig. 1c), which is indicative of the significant improvement of our new model for the prediction of REE and Y partitioning in low-Ca pyroxenes. In supplementary Fig. S4, we further compare our global model with each partitioning experiments in Omuna diagrams.

Sixfold versus eightfold coordinated ionic radii of REE

The use of eightfold coordinated ionic radii in our application of the lattice strain model needs an explanation. Orthopyroxene has a larger sixfold M2 site and a smaller sixfold M1 site. REE and Y preferentially substitute into the M2 site of opx. Sixfold coordinated ionic radii have been used in the application of the lattice strain model to REE^{3+} and Y^{3+} partitioning in opx (e.g., Wood and Blundy 2003; Frei et al. 2009), a choice that we also made initially in this study. In the supplementary Figs. S3 and S7, we show that indeed sixfold coordinated ionic radii work very well for both our measured partitioning data and the global fit to our filtered 344 data. However, when comparing our low-Ca partitioning model (Eqs. 1, S1–S3) with the cpx model of Sun and Liang (2012), it became clear that the sixfold coordinated ionic radius of Pr reported in Shannon (1976) might not be as accurate as it should be. This is shown in Fig. 9 where Pr appears to deviate slightly from the nearly linear trend defined by the rest of REE and Y. According to Shannon (1976), ionic radius of sixfold Pr is an interpreted value based on an approximately linear correlation between ionic volumes (r^3) and unit cell volumes (V) of isotypic series of oxides and fluorides. Although the small deviation of the sixfold ionic radius of Pr does not affect the overall quality of the fits to the lattice strain model for low-Ca pyroxene (Figs. S3 and S7), it does result in an unphysical kink in the calculated REE opx-cpx partition coefficients in the otherwise smooth spider diagram (see supplementary Fig. S9). One way to resolve this inconsistency is to use eightfold coordinated ionic radii of REE and Y reported in Shannon (1976) as proxies for the sixfold coordinated ionic radii in the lattice strain model

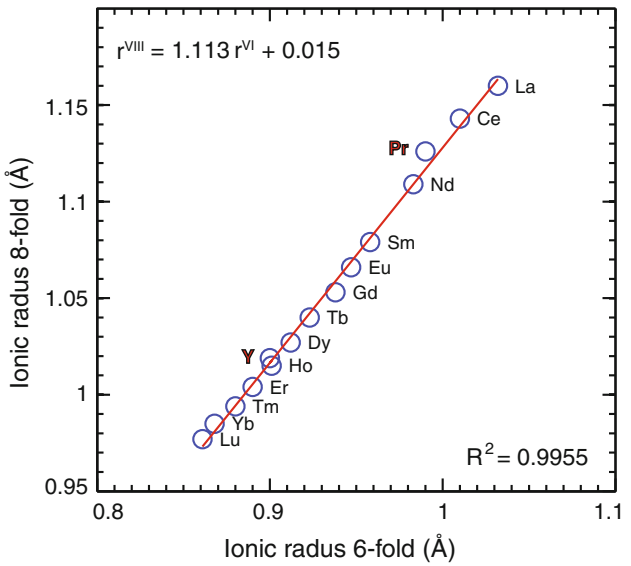

Fig. 9 Correlation between sixfold and eightfold coordinated ionic radii (r^{VI} and r^{VIII}) for REE and Y. Ionic radii are from Shannon (1976)

for low-Ca pyroxene. This does not imply that REE is in eightfold coordination in the M2 site of low-Ca pyroxene, but an interim solution to this peculiar problem. Given the nearly linear correlation between the two sets of ionic radii (Fig. 9), the use of eightfold coordinated ionic radii merely results in a change in numerical values of the fitting parameters in the lattice strain model (c.f. Eqs. 11–13, S1–S3). The unphysical kink in the spider diagram disappeared (c.f. Figs. 14, S9) when eightfold coordinated ionic radii were used.

Composition dependence of REE partitioning in pyroxene

Our model indicates that REE and Y partition coefficients strongly depend on both temperature and X_{Ca}^{M2} and X_{Al}^{T} in low-Ca pyroxene. Temperature and pyroxene composition have opposite or competing effects (Eq. 11), a point that will be discussed in a later section. According to Eq. (2), REE partitioning in cpx is controlled primarily by X_{Al}^{T} and X_{Mg}^{M2} in cpx. Figure 10a–i compares Ce, Nd, and Yb partitioning coefficients as functions of X_{Al}^{T}, X_{Ca}^{M2}, and X_{Mg}^{M2} in pyroxenes from the filtered data of Sun and Liang (2012) and those used in the present study (red squares for opx and green diamonds for subcalcic augite). The effects of X_{Al}^{T} on REE partitioning are similar among the three pyroxenes (i.e., similar slopes in Fig. 10a–c), while the effect of X_{Ca}^{M2} appears more important in low-Ca pyroxene than in cpx. This is consistent with the large coefficient of X_{Ca}^{M2} in Eq. (11). The partition coefficients for low-Ca pyroxene negatively correlate with X_{Mg}^{M2} (Fig. 10g–i), which may be explained by the complementary relationship between X_{Ca}^{M2} and X_{Mg}^{M2} on the M2 site. REE and Y partition coefficients are inversely correlated with temperature, but not explicitly dependent on pressure or melt composition (c.f. Eq. 11). Since the major element compositions of low-Ca pyroxene and melt vary systematically as a function of pressure and temperature, pressure (and melt compositions) can indirectly affect the partition coefficients of REE and Y between pyroxene and melt through the mineral compositions. The strain-free lattice size (r_0) increases with the increase of X_{Ca}^{M2} and X_{Mg}^{M2} in low-Ca pyroxene according to Eq. (12). The factors are different from those for cpx where r_0 decreases with increasing X_{Al}^{M1} and X_{Mg}^{M2} in cpx (c.f. Eqs. 3, 12). This difference may account for the X_{Ca}^{M2} dependence of E, which is absent in the cpx model of Sun and Liang (2012, c.f. Eqs. 4, 13).

The effect of water on REE partitioning in low-Ca pyroxene

Partitioning studies have indicated that presence of water in the melt hinders REE partitioning in cpx and garnet (Wood and Blundy 2003; Green et al. 2000; Adam and Green 2006; Sun and Liang 2012). To investigate the effect of water on REE partitioning in low-Ca pyroxene, we incorporated water in our parameterization following the procedure of Sun and Liang (2012). A preliminary model incorporating water effect can be found in the supplementary material (Fig. S8). The preliminary hydrous model has a χ_P^2 value of 1.31 (1.30 for anhydrous model). Hence, including water as an additional variable does not improve the goodness of fit. The very small coefficient of water (an order of magnitude smaller than the coefficients of X_{Ca}^{M2} and X_{Al}^{T}) and large standard deviation (>100 %) also suggest that the effect of water on REE partitioning in low-Ca pyroxene is insignificant. Since only three partitioning experiments in our compiled data set were conducted under hydrous conditions (Green et al. 2000; McDade et al. 2003b; Adam and Green 2006), water effect may not be fully quantified in our preliminary model. Additional hydrous partitioning experiments are needed to further investigate the effect of water on trace element partitioning in low-Ca pyroxene.

REE and Y partitioning between subsolidus opx and cpx: a field test

The excellent agreement between partition coefficients for REE and Y in low-Ca pyroxene calculated using our parameterized model and experimentally measured values from the filtered data set is very encouraging (Fig. 8). To further test the validity of the assumptions and approximations used in our model development, we conducted a

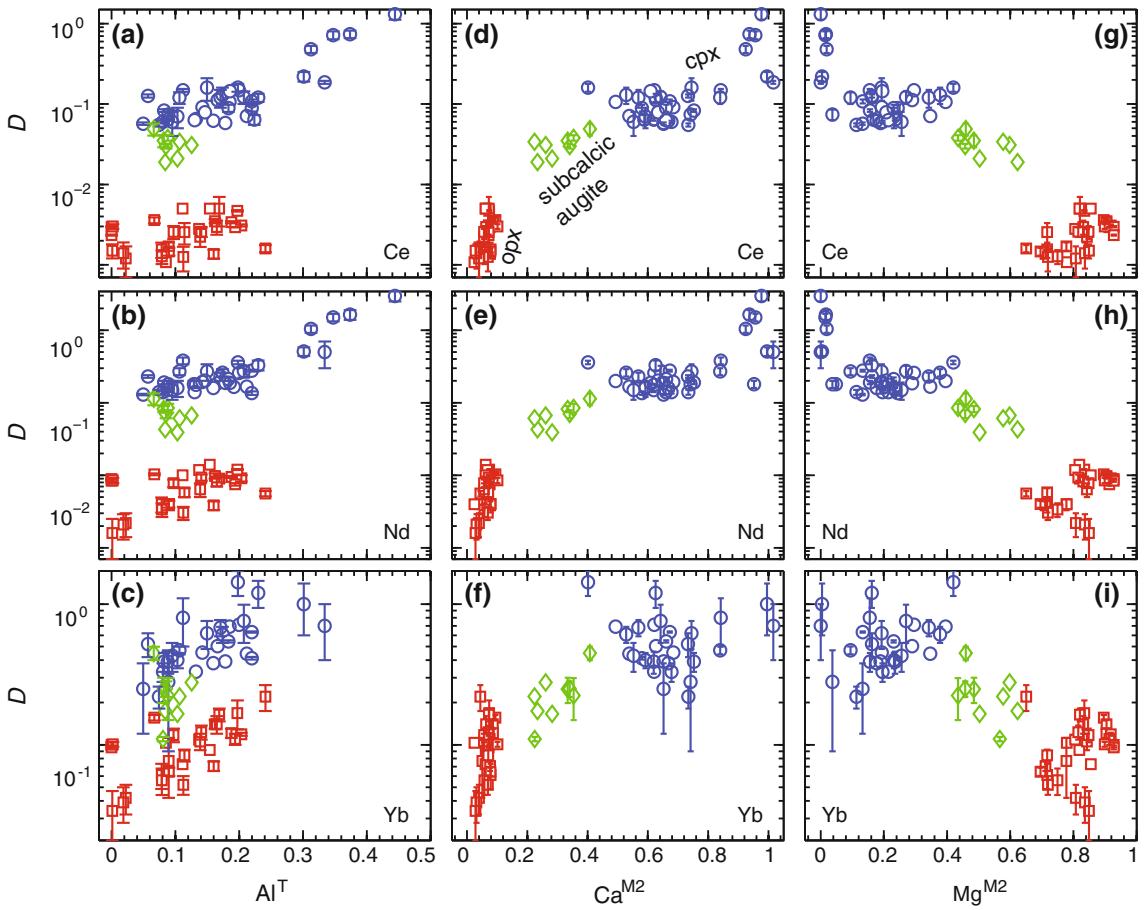

Fig. 10 Variation of selected REE partition coefficients in low-Ca and high-Ca pyroxenes as functions of Al content on the tetrahedral site (X^{T}_{Al}), and Ca and Mg abundances on the M2 site (X^{M2}_{Ca} and X^{M2}_{Mg}, respectively) of pyroxene. Data source and symbols are the same as those in Fig. 7

field test. Witt-Eickschen and O'Neill (2005) and Witt-Eickschen et al. (2009) measured the abundance of REE and other trace elements in cpx and opx from two suites of well-equilibrated spinel lherzolite xenoliths (866–1,262 °C) using LA-ICP-MS. They showed that opx-cpx partition coefficients for REE and Y vary systematically as a function of temperature and mineral compositions. To independently test our parameterized models for REE and Y partitioning in low-Ca pyroxene and high-Ca pyroxene, we calculated opx-cpx partition coefficients for REE and Y using the major element compositions reported in Witt-Eickschen and O'Neill (2005) and Witt-Eickschen et al. (2009), and our low-Ca and high-Ca pyroxene partitioning models (Eqs. 1–4, 11–13). The equilibrium temperatures were calculated using the cpx-opx geothemometry of Brey and Köhler (1990). Figure 11 shows very good to excellent agreements between our model-derived opx-cpx partition coefficients and those reported in Witt-Eickschen and O'Neill (2005) and Witt-Eickschen et al. (2009). The deviation of some D_{La} from the main trend (two from Witt-Eickschen and O'Neill 2005 and five from Witt-Eickschen et al. 2009) is possibly due to the very low abundances of La in opx and large analytical uncertainties. Figure 11 also compares the model-derived and LA-ICP-MS-measured opx-cpx partition coefficients of REE and Y between coexisting opx and cpx in a lherzolite and a harzburgite reported by Eggins et al. (1998). Again, there is an excellent agreement between our model results and the measured data.

It is worth noting that the application of our parameterized models to REE partitioning between opx and cpx in peridotite xenoliths is an *extrapolation*, as these models were calibrated at magmatic conditions. The very good to excellent agreement between the model-predicted and observed values for the subsolidus peridotites demonstrates the internal consistency between the partitioning models for REE and Y in low-Ca pyroxene (this study) and high-Ca pyroxene (Sun and Liang 2012) and further justifies the assumptions and simplifications made in our parameterization and the lattice strain model. The model validations

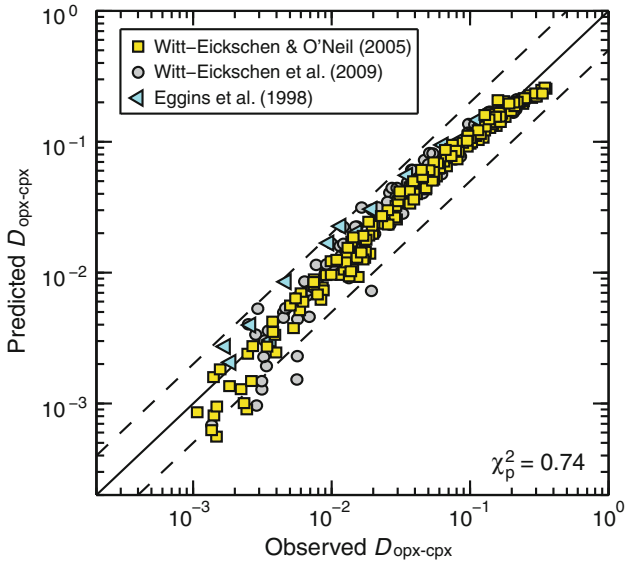

Fig. 11 Comparison between model-derived and observed REE partition coefficients for opx-cpx. Observed data are from well-equilibrated spinel lherzolite and harzburgite xenoliths of Witt-Eickschen and O'Neill (2005), Witt-Eickschen et al. (2009), and Eggins et al. (1998). Trace element abundances in these xenoliths were analyzed by LA-ICP-MS. Predicted values are calculated using Eqs. (1)–(4), (11)–(13)

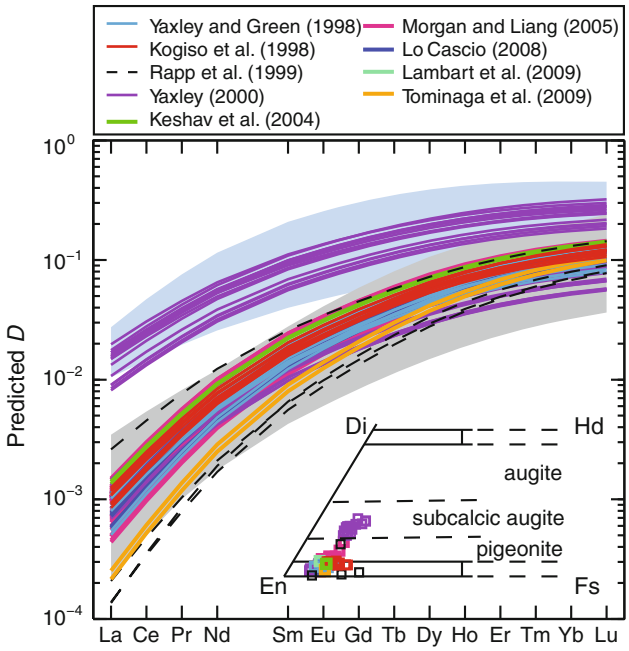

Fig. 12 Model-predicted REE partition coefficients for low-Ca pyroxenes produced by pyroxenite-derived melt and peridotite interactions. Partition coefficients are calculated using Eqs. (1), (11)–(13), and experimental temperatures and major element compositions from the references listed in the legend. Major element compositions of the pyroxenes from selected publications are shown in the inset of the pyroxene quadrilateral. The *gray field* represents the range of REE partitioning data for opx, and the *light blue* is the range of subcalcic augite, both of which are defined by the filtered data listed in Table 3

presented above and discussed in Sun and Liang (2012) give additional assurance in their applications to REE fractionation during mantle melting, melt-rock interaction, and magma differentiation processes. To apply our two-pyroxene partitioning models to subsolidus samples, two conditions must be met: (1) peridotite samples must be well equilibrated and free of secondary processes; (2) the temperature of equilibration is calculated using the cpx-opx thermometer of Brey and Köhler (1990). Application of the Ca-in-opx thermometer of Brey and Köhler (1990) results in an overestimation of opx-cpx partition coefficients for REE and Y. This may be due to the differences between the two thermometers, as the Ca-in-opx thermometer tends to give lower temperature (up to 20–100 °C) than the cpx-opx thermometer. For well-equilibrated mafic and ultramafic samples, our two-pyroxene partitioning models may be used as a thermometer, a topic that will be explored in the future.

Applications

As shown in Figs. 5 and 10, REE and Y partition coefficients in low-Ca pyroxene vary considerably. In this section, we examine the importance of these variations in relation to geochemical modeling of adiabatic mantle melting and pyroxenite-derived melt and peridotite interaction in the mantle.

Partitioning of REE in low-Ca pyroxene during pyroxenite-derived melt and peridotite interaction

Reaction between pyroxenite-derived melt and peridotite can generate low-Ca pyroxenes. This process is particularly effective at depths just above the peridotite solidus where melt derived from pyroxenite can readily infiltrate into partially molten lherzolite (Lo Cascio 2008). Depending on the reacting melt composition, major element compositions of the reacted low-Ca pyroxene can vary considerably (see inset to Fig. 12). Partitioning of REE in low-Ca pyroxene during pyroxenite-derived melt and peridotite interaction is likely a function *P-T-X*, a topic that has not been examined previously. To investigate the variation of REE partitioning in low-Ca pyroxenes produced by melt-rock reaction, we calculated REE partition coefficients using temperature and major element compositions of the pyroxene reported in the melt-rock reaction experiments and our parameterized lattice strain model (Eqs. 1, 11–13), with the results shown in Fig. 12. Partitioning values for these pyroxenes, especially those of light REE (LREE), are distributed over a relatively wide range, suggesting a strong dependence on

temperature and pyroxene composition. In general, predicted LREE partition coefficients in subcalcic augite from high-pressure experiments of Yaxley (2000) are more than an order of magnitude higher than those of opx. However, not all pyroxenes formed via melt-rock reaction have higher partition coefficients, examples being those low partition coefficients derived from three experiments of Rapp et al. (1999). Exceptionally low Ca and Al abundances in opx in the latter study (CaO = 0.17–0.68 %; Al_2O_3 = 0.33–2.25 %, compared with the general range of CaO = 1.5–2.7 %; Al_2O_3 = 3.3–9.0 %) are the main reason. Hence, the composition of the (starting) pyroxenite or eclogite is important in determining the composition of low-Ca pyroxene, which in turn controls REE partitioning in opx or subcalcic augite at a given temperature and pressure. As will be further demonstrated below, partition coefficients of REE in opx derived from pyroxenite-derived melt and peridotite interactions can be significantly different from those in opx in lherzolite along a mantle adiabat.

REE partitioning in orthopyroxene along mantle adiabats

During adiabatic mantle melting, both temperature and pyroxene composition vary systematically as a function of pressure or depth. Here, we examine variations in REE partition coefficients between opx and basaltic melts during adiabatic mantle melting. We consider three cases of different potential temperatures (T_P) using either the depleted MORB mantle (DMM) of Workman and Hart (2005) or an enriched mantle (EM) composed of 90 % DMM and 10 % N-MORB (composition from Hofmann 1988) as our starting mantle compositions: (1) T_P = 1,300 °C and DMM source (Fig. 13a–c); (2) T_P = 1,400 °C and DMM source (Fig. 13d–f); and (3) T_P = 1,350 °C and EM source (Fig. 13g–i). Similar to Sun and Liang (2012), we calculated the compositions of residual opx using pMELTS (Ghiorso et al. 2002) and partition coefficients using Eqs. (1), (11)–(13). Figure 13 summarizes the calculated opx compositions and REE partition coefficients. (A similar figure showing the variations of major element compositions and REE partition coefficients for coexisting cpx can be found in supplementary Fig. S1.)

For the case of T_P = 1,300 °C and DMM, melting begins in the spinel lherzolite stability field. As the temperature decreases, X^{M2}_{Ca} in opx increases, whereas X^{T}_{Al} in opx decreases (Fig. 13a). According to Eq. (11), X^{T}_{Al} has a competing effect with X^{M2}_{Ca} and temperature on REE partitioning in opx in the spinel lherzolite. Since the decrease of X^{T}_{Al} is larger than the increase of X^{M2}_{Ca} in opx, the net result is a relatively constant partition coefficient for REE along the 1,300 °C adiabat (Fig. 13b). After cpx has been consumed, both X^{M2}_{Ca} and X^{T}_{Al} in opx decrease with decreasing temperature, so that temperature now has a competing effect with both X^{M2}_{Ca} and X^{T}_{Al} in opx on REE partitioning. The net effect is a very small decrease in REE partition coefficients along the cpx-free portion of the adiabat. The overall effect of changing temperature, X^{M2}_{Ca}, and X^{T}_{Al} in opx along the 1,300 °C mantle adiabat is very small, so that variations in REE partition coefficients in opx are in a very small range over the entire melting interval (Fig. 13c).

For the case of T_P = 1,400 °C and DMM, melting starts in the garnet stability field. Figure 13d and e shows variations of X^{M2}_{Mg}, X^{M2}_{Ca}, and X^{T}_{Al} in opx and partition coefficients along the mantle adiabat. Before garnet has been consumed, as temperature decreases, X^{T}_{Al} increases while X^{M2}_{Ca} remains approximately constant, so that the effects of temperature and X^{T}_{Al} effectively cancel out. Variations of partition coefficients after garnet is consumed behave the same way as those in spinel lherzolite and cpx-bearing harzburgite as discussed in the first example. To a good approximation, partition coefficients of REE in opx in the garnet and spinel lherzolite and cpx-bearing harzburgite can be taken as constants along this mantle adiabat. However, after cpx has been consumed, both X^{M2}_{Ca} and X^{T}_{Al} in opx decrease with decreasing temperature. The decrease is more significant than those in case (1), so larger variations in REE partition coefficients are observed, especially in LREE (Fig. 13e, f). REE partition coefficients in opx in cpx-free harzburgite cannot be taken as constants in this latter case.

For the case of T_P = 1,350 °C and EM, melting also begins in the garnet stability field. Figure 13g–i shows that opx composition and calculated REE partition coefficients fall in between values from cases (1) and (2). This simulation shows that the starting lherzolite composition has only a very small effect on the calculated REE partition coefficients in the garnet and spinel lherzolite and cpx-bearing harzburgite.

In summary, partition coefficients of REE in opx can be treated as constants along a mantle adiabat at a given potential temperature and mantle source composition as long as cpx is present in the residue and the major element composition of opx calculated from pMELTS can be treated as accurate. Variations of REE partition coefficients in opx (green fields in Fig. 13c, f, i) happen predominantly in the cpx-free harzburgite and have to be taken into consideration in trace element modeling of mantle melting and melt migration. For convenience, we list our recommended opx-melt and cpx-melt partition coefficients along three different mantle adiabats in Table 4, which are the average values for garnet and spinel lherzolites and cpx-bearing harzburgite. The average partition coefficients of opx and those of cpx from Table 4 are used to calculate opx-cpx

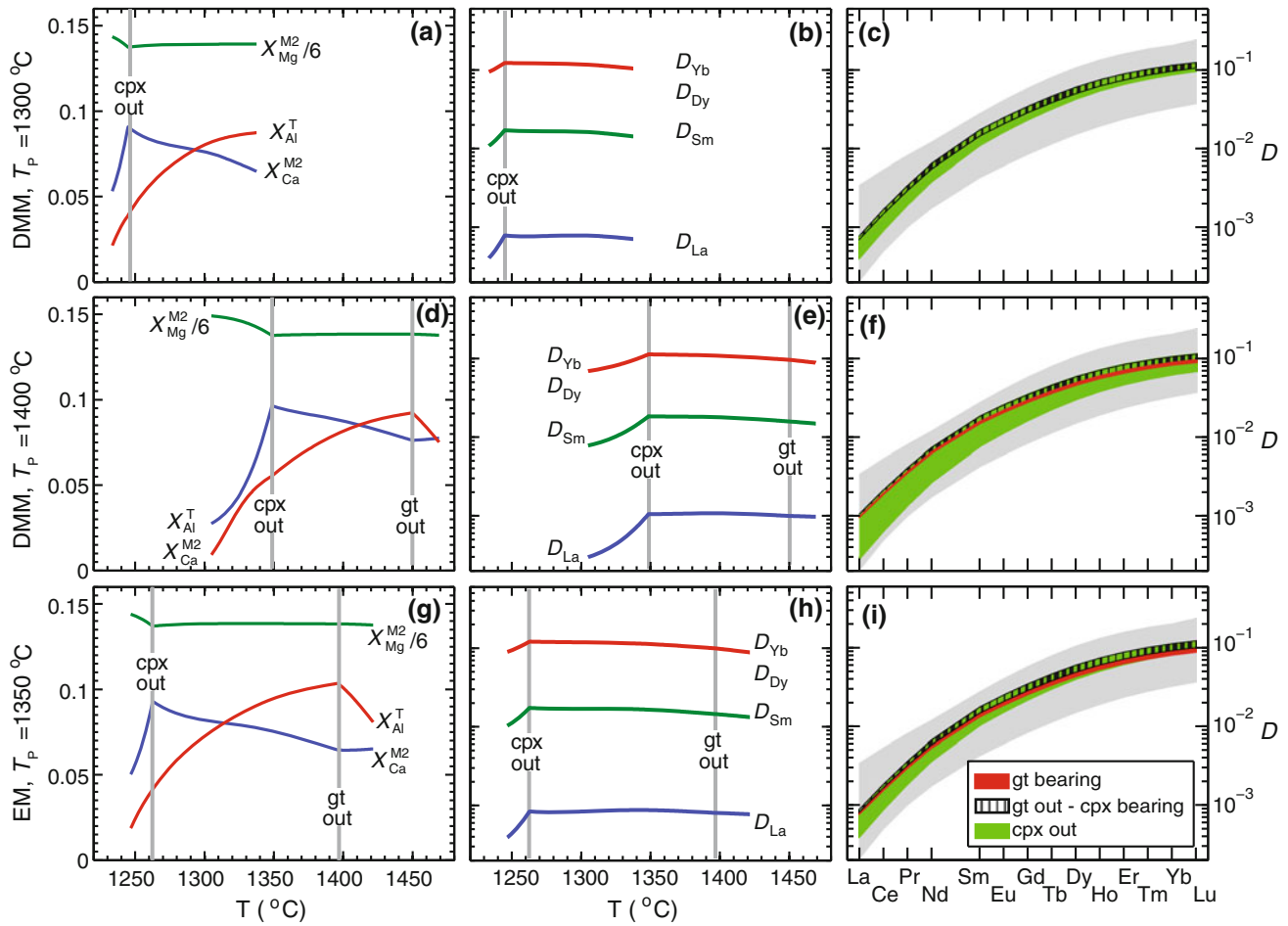

Fig. 13 Variations of X^{M2}_{Ca}, X^{T}_{Al}, and X^{M2}_{Mg} and calculated REE partition coefficients in opx along three mantle adiabats (T_p = 1,300, 1,350, and 1,400 °C) and for two choices of starting mantle composition (DMM and EM). T_p is the mantle potential temperature; DMM is the depleted MORB mantle from Workman and Hart (2005); EM is an assumed enriched mantle composition that consists of 90 % DMM + 10 % N-MORB. Composition of N-MORB is from Hofmann (1988). Orthopyroxene compositions were calculated using pMELTS (Ghiorso et al. 2002), and the corresponding REE partition coefficients were calculated using our parameterized lattice strain model for low-Ca pyroxene (Eqs. 1, 11–13). *Gray fields* in (**c**), (**f**), and (**i**) represent the ranges of measured REE partition coefficients defined by the filtered data (Table 3). gt represents garnet. See text for "Discussion"

partition coefficients along two mantle adiabats (T_p = 1,300 and 1,400 °C, DMM). Figure 14 compares our calculated REE opx-cpx partition coefficients along the two mantle adiabats with the recommended values of Lee et al. (2007) for isothermal mantle melting at 1,300 and 1,400 °C. The most important difference between adiabatic and isothermal cases is in the LREE: During adiabatic mantle melting, orthopyroxene is likely to play a greater role in fractionating LREE than commonly believed.

Conclusions

Partition coefficients for trace elements in low-Ca pyroxene produced by pyroxenite-derived melt and peridotite interactions were determined experimentally at 1,340–1,425 °C and 2 GPa. Based on a combination of these new partitioning results and a subset of published low-Ca pyroxene partitioning data, we developed a parameterized lattice strain model for REE and Y partitioning between low-Ca pyroxene and basaltic melt over a large range of *P-T-X*. By combining our model with a recent model for REE and Y partitioning in high-Ca pyroxene that was calibrated using a similar method (Sun and Liang 2012), we demonstrated very good to excellent agreement between the model-derived and independently measured opx-cpx partition coefficients for REE and Y in well-equilibrated peridotite xenoliths. This agreement not only justifies the assumptions and simplifications made in the development of our models but also lends added assurance to the model applications to REE fractionation

Table 4 Recommended REE partition coefficients for adiabatic melting of anhydrous diopside-bearing peridotite

T_p	DMM[a]				EM[b]	
	1,300 °C		1,400 °C		1,350 °C	
D	opx[c]	cpx[d]	opx[c]	cpx[d]	opx[c]	cpx[d]
La	0.0007	0.0466	0.001	0.0449	0.0008	0.0484
Ce	0.0015	0.0733	0.0019	0.0666	0.0016	0.0741
Pr	0.003	0.1093	0.0036	0.0947	0.0032	0.1081
Nd	0.0055	0.1544	0.0065	0.1291	0.0058	0.1505
Sm	0.0143	0.2510	0.0156	0.2023	0.0146	0.2415
Eu	0.0204	0.2952	0.0217	0.2367	0.0206	0.2841
Gd	0.0281	0.3377	0.0293	0.2710	0.0282	0.3258
Tb	0.0376	0.3758	0.0383	0.3035	0.0374	0.3647
Dy	0.0487	0.4071	0.0487	0.3329	0.0481	0.3987
Ho	0.0601	0.4283	0.0591	0.3560	0.0592	0.424
Er	0.0714	0.4402	0.0692	0.3729	0.0699	0.441
Tm	0.0819	0.4443	0.0784	0.3842	0.0800	0.4508
Yb	0.0913	0.4426	0.0865	0.3909	0.0891	0.4548
Lu	0.0995	0.4368	0.0935	0.3939	0.0969	0.4545

[a] DMM is the depleted MORB mantle source from Workman and Hart (2005)

[b] EM is an assumed enriched mantle composition that is composed of 90 % DMM and 10 % N-MORB in major element compositions, and N-MORB is from Hofmann (1988)

[c] opx partition coefficients are the average values of those from garnet lherzolite to spinel lherzolite and cpx-bearing harzburgite stability field during adiabatic melting

[d] cpx partition coefficients for the DMM source are from Sun and Liang (2012), or average values calculated using Eqs. (1)–(4) for the EM source along the 1,350 °C adiabat in the spinel stability field

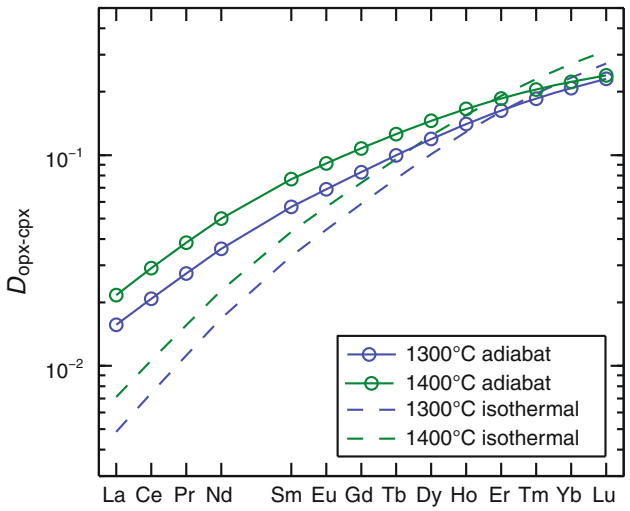

Fig. 14 REE opx-cpx partition coefficients along two mantle adiabats (T_p = 1,300 and 1,400 °C with DMM mantle source, *solid lines*). For comparison, REE opx-cpx partition coefficients from Lee et al. (2007) at constant temperatures of 1,300 and 1,400 °C are also shown (*dashed lines*). $D_{opx-cpx}$ along the two mantle adiabats are calculated using the recommended values for DMM listed in Table 4

during mantle melting, melt-rock interaction, and magma differentiation processes. The main conclusions of this paper are as follows:

1. Partition coefficients of REE and Y in low-Ca pyroxene are positively correlated with X_{Ca}^{M2} and X_{Al}^{T} in pyroxene but inversely correlated with temperature, giving rise to a strong competing effect between temperature and low-Ca pyroxene compositions.
2. Partition coefficients of REE and Y in low-Ca pyroxene produced by pyroxenite-derived melt and peridotite interaction span almost the entire range defined by the published low-Ca pyroxene partitioning data. Major element compositions of pyroxenite and temperature must be considered when selecting REE partition coefficients for low-Ca pyroxenes derived from melt-rock reaction.
3. In the presence of cpx, the competing effect between temperature and opx composition results in very small variations in REE and Y partition coefficients in opx along a mantle adiabat. Constant partition coefficients can be used for REE and Y in opx during decompression melting of lherzolite and cpx-bearing harzburgite. However, in the absence of cpx, partition coefficients of LREE vary considerably, and the variations should be taken into consideration when modeling REE fractionation during high-degree melting of cpx-free harzburgite.

4. The very good to excellent agreement between the model-derived and independently measured opx-cpx partition coefficients for REE and Y in the three suites of well-equilibrated peridotite xenoliths suggests that our two pyroxene partitioning models may be used as a thermometer.

Acknowledgments We wish to thank Nick Dygert, Katie Kelley, and Marion Lytle for their help and advice in LA-ICP-MS analysis. Amanda Getsinger, Colin Jackson, and Nick Dygert read an earlier version of this manuscript and made many useful suggestions. The manuscript benefited from thoughtful comments and suggestions from two anonymous reviewers and the editor Tim Grove. This work was supported in part by NSF grants EAR-0911501 and EAR-0738734, and NASA grant NNX09AE33G.

References

Adam J, Green T (2006) Trace element partitioning between mica- and amphibole-bearing garnet lherzolite and hydrous basanitic melt: 1. Experimental results and the investigation of controls on partitioning behavior. Contrib Mineral Petrol 152:1–17

Bédard JH (2007) Trace element partitioning coefficients between silicate melts and orthopyroxene: parameterizations of D variations. Chem Geol 244:263–303

Blundy JD, Wood BJ (1994) Prediction of crystal-melt partition coefficients from elastic moduli. Nature 372:452–454

Brey GP, Köhler T (1990) Geothermobarometry in four-phase lherzolites II, New thermobarometers, and practical assessment of existing thermobarometers. J Petrol 31:1353–1378

Brice JC (1975) Some thermodynamic aspects of the growth of strained crystals. J Crystal Growth 28:249–253

Colson RO, McKay GA, Taylor LA (1988) Temperature and composition dependencies of trace element partitioning: Olivine/melt and low-Ca pyroxene/melt. Geochim Cosmochim Acta 52:539–553

Eggins SM, Rudnick RL, McDonough WF (1998) The composition of peridotites and their minerals: a laser-ablation ICP-MS study. Earth Planet Sci Lett 154:53–71

Frei D, Liebscher A, Franz G, Wunder B, Klemme S, Blundy J (2009) Trace element partitioning between orthopyroxene and anhydrous silicate melt on the lherzolite solidus from 1.1 to 3.2 GPa and 1230 to 1535 °C in the model system Na2O-CaO-MgO-Al2O3-SiO2. Contrib Mineral Petrol 157:473–490

Ghiorso MS, Hirschmann MM, Reiners PW, Kress VC (2002) The pMELTS: a revision of MELTS for improved calculation of phase relations and major element partitioning related to partial melting of the mantle to 3 GPa. Geochem Geophys Geosyst 3. doi:10.1029/2001GC000217

Green TH, Blundy JD, Adam J, Yaxley GM (2000) SIMS determination of trace element partition coefficients between garnet, clinopyroxene and hydrous basaltic liquids at 2–7.5 GPa and 1080–1200 °C. Lithos 53:165–187

Hirschmann MM, Kogiso T, Baker MB, Stolper EM (2003) Alkalic magmas generated by partial melting of garnet pyroxenite. Geology 31:481–484

Hofmann AW (1988) Chemical differentiation of the Earth: the relationship between mantle, continental crust, and oceanic crust. Earth Planet Sci Lett 90:297–314

Jochunm KP, Stoll B, Herwig K et al (2006) MPI-DING reference glasses for in situ microanalysis: New reference values for element concentrations and isotope ratios. Geochem Geophys Geosyst 7:Q02008. doi:10.1029/2005GC001060

Kelley KA, Plank T, Ludden J, Staudigel H (2003) Composition of altered oceanic crust at ODP sites 801 and 1149. Geochem Geophys Geosyst 4:8910. doi:10.1029/2002GC000435

Kennedy AK, Lofgren GE, Wasserburg GJ (1993) An experimental study of trace element partitioning between olivine, orthopyroxene and melt in chondrules: equilibrium values and kinetic effects. Earth Planet Sci Lett 115:177–195

Keshav S, Gudfinnsson GH, Sen G, Fei Y (2004) High-pressure melting experiments on garnet clinopyroxenite and the alkalic to tholiitic transition in ocean-island basalts. Earth Planet Sci Lett 223:365–379

Klemme S, Blundy JD, Wood BJ (2002) Experimental constraints on major and trace element partitioning during partial melting of eclogite. Geochim Cosmochim Acta 66:3109–3123

Klemme S, Günther D, Hametner K, Prowatke S, Zack T (2006) The partitioning of trace elements between ilmenite, ulvöspinel, armalcolite and silicate melts with implications for the early differentiation of the moon. Chem Geol 234:251–263

Kogiso E, Hirschmann MM (2006) Partial melting experiments of bimineralic eclogite and the role of recycled mafic oceanic crust in the genesis of ocean island basalts. Earth Planet Sci Lett 249:188–199

Kogiso T, Hirose K, Takahashi E (1998) Melting experiments on homogeneous mixtures of peridotite and basalt: application to the genesis of ocean island basalts. Earth Planet Sci Lett 162:45–61

Kogiso T, Hirschmann MM, Frost DJ (2003) High-pressure partial melting of garnet pyroxenite: possible mafic lithologies in the source of ocean island basalts. Earth Planet Sci Lett 216:603–617

Lambart S, Laporte D, Schiano P (2009) An experimental study of pyroxenite partial melts at 1 and 1.5 GPa: Implications for the major-element composition of Mid-Ocean Ridge Basalts. Earth Planet Sci Lett 288:335–347

Lee CA, Harbert A, Leeman WP (2007) Extension of lattice strain theory to mineral/mineral rare-earth element partitioning: An approach for assessing disequilibrium and developing internally consistent partition coefficients between olivine, orthopyroxene, clinopyroxene and basaltic melt. Geochim Cosmochim Acta 71:481–496

Lo Cascio M (2008) Kinetics of partial melting and melt-rock reaction in the earth's mantle. Ph.D. dissertation, Brown University

Lo Cascio M, Liang Y (2007) Reaction between lherzolite and eclogite-derived melts in the upper mantle. EOS Trans. Fall AGU, DI43A-08

McDade P, Blundy JD, Wood BJ (2003a) Trace element partitioning on the Tinaquillo Lherzolite solidus at 1.5 GPa. Phys Earth Planet Inter 139:129–147

McDade P, Blundy JD, Wood BJ (2003b) Trace element partitioning between mantle wedge peridotite and hydrous MgO-rich melt. Am Mineral 88:1825–1831

Médard E, McCammon CA, Barr JA, Grove TL (2008) Oxygen fugacity, temperature reproducibility, and H_2O contents of nominally anhydrous piston-cylinder experiments using graphite capsules. Am Mineral 93:1838–1844

Morgan Z, Liang Y (2005) An experimental study of the kinetics of lherzolite reactive dissolution with applications to melt channel formation. Contrib Mineral Petrol 150:369–385

Pearce NJG, Perkins WT, Westgate JA, Gorton MP, Jackson SE, Neal CR, Chenery SP (1997) A compilation of new and published major and trace element data for NIST SRM 610 and NIST SRM 612 glass reference materials. Geostand Newslett 21:115–144

Pertermann M, Hirschmann MM (2003a) Partial melting experiments on a MORB-like pyroxenite between 2 and 3 GPa: Constraints on the presence of pyroxenite in basalt source regions from solidus location and melting rate. J Geophys Res 108:2125–2142

Pertermann M, Hirschmann MM (2003b) Anhydrous partial melting experiments on MORB-like eclogite: phase relations, phase compositions and mineral-melt partitioning of major elements at 2–3 GPa. J Petrol 44:2173–2201

Rapp RP, Shimizu N, Norman MD, Applegate GS (1999) Reaction between slab-derived melts and peridotite in the mantle wedge: experimental constraints at 3.8 GPa. Chem Geol 160:33–356

Salters VJM, Longhi J (1999) Trace element partitioning during the initial stages of melting beneath mid-ocean ridges. Earth Planet Sci Lett 166:15–30

Salters VJM, Longhi JE, Bizimis M (2002) Near mantle solidus trace element partitioning at pressures up to 3.4 GPa. Geochem Geophys Geosyst 3. doi:10.1029/2001GC000148

Schwandt CS, MaKay GA (1998) Rare earth element partition coefficients from enstatite/melt synthesis experiments. Geochim Cosmochim Acta 62:2845–2848

Seber GAF, Wild CJ (1989) Nonlinear regression. Wiley, New York

Shannon RD (1976) Revised effective ionic radii and systematic studies of interatomic distances in halides and chalcogenides. Acta Cryst A32:71–767

Snyder GA, Taylor LA, Neal CR (1992) A chemical-model for generating the sources of Mare basalts-combined equilibrium and fractional crystallization of the lunar magmasphere. Geochim Cosmochim Acta 56:3809–3823

Spandler C, Yaxley G, Green DH, Rosenthal A (2008) Phase relations and melting of anhydrous K-bearing eclogite from 1200 to 1600 °C and 3 to 5 GPa. J Petrol 49:771–795

Sun C, Liang Y (2012) Distribution of REE between clinopyroxene and basaltic melt along a mantle adiabat: Effects of major element composition, water and temperature. Contrib Mineral Petrol. doi:10.1007/s00410-011-0700-x

Sun C, Yao L, Liang Y (2011) Some speculations on the distribution of REE between orthopyroxene and lunar picritic glass melts at multiple-saturation points. Lunar Planet Sci XXXXII, abstract #2009

Takahashi E, Nakajima K (2002) Melting process in the Hawaiian Plume: An Experimental Study. Hawaiian Volca 128:403–418

Takahashi E, Nakajima K, Wright TL (1998) Origin of the Columbia River basalts: melting model of a heterogeneous plume head. Earth Planet Sci Lett 162:63–80

Tominaga A, Kato T, Kubo T, Kurosawa M (2009) Preliminary analysis on the mobility of trace incompatible elements during the basalt and peridotite reaction under uppermost mantle conditions. Phys Earth Planet Inter 174:50–59

Tuff J, Gibson SA (2007) Trace-element partitioning between garnet, clinopyroxene and Fe-rich picritic melts at 3 to 7 GPa. Contrib Mineral Petrol 153:369–387

van Kan Parker M, Liebscher A, Frei D, van Sijl J, van Westrenen W, Blundy J, Franz G (2010) Experimental and computational study of trace element distribution between orthopyroxene and anhydrous silicate melt: substitution mechanisms and the effect of iron. Contrib Mineral Petrol 159:459–473

van Kan Parker M, Mason PRD, van Westrenen W (2011) Experimental study of trace element partitioning between lunar orthopyroxene and anhydrous silicate melt: Effects of lithium and iron. Chem Geol 285:1–14

van Westrenen W, Blundy JD, Wood BJ (2000) Effect of Fe^{2+} on garnet-melt trace element partitioning: experimental in FCMAS and quantification of crystal-chemical controls in natural systems. Lithos 53:189–201

Witt-Eickschen G, O'Neill HSC (2005) The effect of temperature on the equilibrium distribution of trace elements between clinopyroxene, orthopyroxene, olivine and spinel in upper mantle peridotite. Chem Geol 221:65–101

Witt-Eickschen G, Palme H, O'Neill HSC, Allen CM (2009) The geochemistry of the volatile trace elements As, Cd, Ga, In and Sn in the Earth's mantle: New evidence from in situ analyses of mantle xenoliths. Geochim Cosmochim Acta 73:1755–1778

Wood BJ, Blundy JD (1997) A predictive model for rare earth element partitioning between clinopyroxene and anhydrous silicate melt. Contrib Mineral Petrol 129:166–181

Wood BJ, Blundy JD (2002) The effect of H_2O on crystal-melt partitioning of trace elements. Geochim Cosmochim Acta 66:3647–3656

Wood BJ, Blundy JD (2003) Trace element partitioning under crustal and uppermost mantle conditions: the influences of ionic radius, cation charge, pressure and temperature. In: Carlson RW (ed) The mantle and core. Treatise Geochem 2:395-424

Workman PK, Hart SR (2005) Major and trace element composition of the depleted MORB mantle (DMM). Earth Planet Sci Lett 231:53–72

Yaxley GM (2000) Experimental study of the phase and melting relations of homogeneous basalt + peridotite mixtures and implications for the petrogenesis of flood basalts. Contrib Mineral Petrol 139:326–338

Yaxley GM, Green DH (1998) Reactions between eclogite and peridotite: mantle refertilisation by subduction of oceanic crust. Schweiz Mineral Petrogr Mitt 78:243–255

Yaxley GM, Sobolev AV (2007) High-pressure partial melting of gabbro and its role in the Hawaiian magma source. Contrib Mineral Petrol 154:371–380